J. Fluid Mech. (2003), *vol.* 478, *pp.* 257–285.
DOI: 10.1017/S0022112002003488 Printed in the United Kingdom

Large-scale structures in a developed flow over a wavy wall

By AXEL GÜNTHER[1] AND PHILIPP RUDOLF VON ROHR[2]†

[1]Department of Chemical Engineering, Massachusetts Institute of Technology, Cambridge, MA 02139, USA

[2]Institute of Process Engineering, Swiss Federal Institute of Technology (ETH), CH-8092 Zurich, Switzerland

(Received 25 June 2001 and in revised form 10 October 2002)

We address – motivated in part by the findings of Gong *et al.* (1996) and Miller (1995) – the role of streamwise-oriented large-scale structures in a developed flow between a sinusoidal bottom wall and a flat top wall. Particle image velocimetry (PIV) is used to examine the spatial variation of the velocity in different planes of the flow through a water channel with an aspect ratio of 12 : 1. The wave amplitude is equal to one tenth of the wall wavelength, Λ, and Reynolds numbers between 500 and 7300, defined with the bulk velocity and the half-height of the channel, are considered. To examine streamwise-oriented structures, the spanwise variation of the velocity field is studied in a plane parallel to the top wall, and in one that intersects the wavy surface at an uphill location. From a proper orthogonal decomposition (POD) of the streamwise velocity fluctuations, we obtain the dominant eigenfunctions with a characteristic spanwise scale of $O(1.5\Lambda)$, which agrees with the scale of perturbations for the streamwise velocity at laminar conditions. A decomposition of the turbulent velocity field close to the uphill section of the wavy surface reveals smaller structures at a location that coincides with the Reynolds shear stress maximum.

1. Introduction

The mean and turbulence quantities of a developed turbulent flow in a channel with a sinusoidal bottom wall (wavelength Λ) and a flat top wall have been a focus of numerous studies, based on both laboratory and numerical experiments. The interest in this flow configuration is given by its technical relevance, and, even more importantly, its applicability as a reference flow for complex flows.

The objective of this paper is to connect, for the separated flow over waves, characteristic regions that were previously identified in a two-dimensional plane with information on three-dimensional large-scale flow structures. To allow comparisons with direct numerical simulations (DNS), we restrict ourselves to relatively low Reynolds numbers. Figure 1 shows the coordinate system for the considered flow configuration, where x is the direction of the mean flow (parallel to the top wall), y is perpendicular to the top wall, and z is the spanwise coordinate. The corresponding velocity components are denoted u, v and w. Channel flow (CF) and boundary layer (BL) flow measurements are considered. The developed flow is characterized by the ratio of the amplitude $2a$ to the wavelength

$$\alpha = \frac{2a}{\Lambda} \tag{1}$$

† Author to whom correspondence should be addressed: vonrohr@ivuk.mavt.ethz.ch

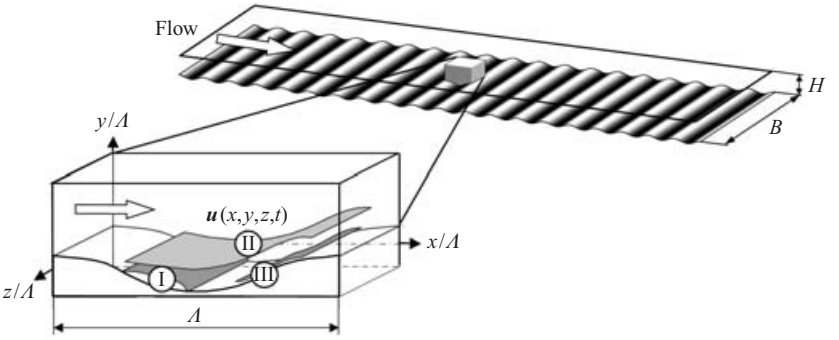

FIGURE 1. Coordinate system and schematic of (I) the regions of separation of the mean flow ($\Psi = 0$), (II) maximum, and (III) minimum Reynolds shear stress (Hudson *et al.* 1996; Cherukat *et al.* 1998).

and the Reynolds numbers

$$Re_h = \frac{U_b h}{\nu} \qquad \text{(CF)}, \qquad Re_\Lambda = \frac{U_\infty \Lambda}{\nu} \qquad \text{(BL flow)}, \tag{2}$$

where ν is the kinematic viscosity of the fluid, h is the half-height of the channel, and U_∞ denotes the free-stream velocity. The bulk velocity U_b is

$$U_b = \frac{\int_{y_w}^{2h} U(x_\xi, y)\,\mathrm{d}y}{\int_{y_w}^{2h} \mathrm{d}y}, \tag{3}$$

where x_ξ denotes an arbitrary x-location and $y_w(x) = 0.05\Lambda\cos(x2\pi/\Lambda)$ describes the profile of the wavy surface. Tables 1 and 2 provide an overview of laboratory experiments, computer simulations and theoretical work on the internal or BL flow over waves, which have been conducted at different Reynolds numbers and for different α.

Mean flow

Early works described the non-separated flow over small-amplitude waves ($\alpha < 0.03$) by linear stability analysis. With increasing ratio α, linear analysis eventually becomes insufficient (Kuzan & Hanratty 1989). Following the original contributions of Motzfeld (1937), Miles (1957), Benjamin (1959), and Hanratty (e.g. Buckles, Hanratty & Adrian 1984), a number of laboratory and recent numerical experiments were conducted to describe the flow field in terms of its mean and turbulence quantities, and the mechanisms for turbulence production. For large enough α and low enough Reynolds numbers, the flow separates (Kuzan & Hanratty 1989) and can be characterized by the following features:

(i) periodicity of the mean flow in the streamwise direction, except for the pressure;
(ii) separation behind the wave crests;
(iii) Reynolds numbers in the range where detailed comparisons with direct numerical simulations (DNS) are possible.

From a regime diagram that was introduced by Kuzan & Hanratty (1989), a time-averaged flow separation can be expected for $Re_h < 30\,000$ for the present case of $\alpha = 0.1$. Characteristic regions of the separated flow are shown in figure 1. A separation zone (I), sometimes referred to as a *separation bubble*, is located in the

References	$Re/1000$	α	Facility	Measurements
Stanton *et al.* (1932)	$23.4, 70.6, 24.0_{\Lambda}$	0.400	WT, A	P_w
Motzfeld (1937)	330_{Λ}	0.050	WT, A	P_w, U
	330_{Λ}	0.100		
Zagustin *et al.* (1966)	147_{Λ}	0.042	CF, W	P_w, U_{crest}
		0.021		
Kendall (1970)	$19-64_{\Lambda}$	0.042	WT, A	P, τ_w, U_i, $\sqrt{\overline{u_i'^2}}$
Sigal (1971)	$154, 306_{\Lambda}$	0.052	WT, A	P, τ_w, U_i, $\sqrt{\overline{u_i'^2}}$
Lees *et al.* (1972)	$154, 306_{\Lambda}$	0.056		
Hsu & Kennedy	57.5_h	0.044	T, A	U, V, $\sqrt{\overline{u'^2}}$, $\sqrt{\overline{v'^2}}$,
(1971)	57.5_h	0.022		$\sqrt{\overline{w'^2}}$, $-\overline{u'v'}$
Beebe (1972)	$21.4-85.6_{\Lambda}$	0.170	WT, A	P, τ_w, U_i, $\sqrt{\overline{u_i'^2}}$
	$21.4-85.6_{\Lambda}$	0.400	WT, A	
Thorsness (1975)	$5.4-30_h$	0.013	CF, W	τ_w
Zilker (1976)	7.0_h	0.013	CF, W	U, V, $\sqrt{\overline{u'^2}}$, $\sqrt{\overline{v'^2}}$, $-\overline{u'v'}$
	7.0_h	0.031	CF, W	U, V, $\sqrt{\overline{u'^2}}$, $\sqrt{\overline{v'^2}}$, $-\overline{u'v'}$
	$6.0-32_h$			τ_w, $\sqrt{\overline{\tau'^2}_w}$
	7.0_h	0.050	CF, W	U, V, $\sqrt{\overline{u'^2}}$, $\sqrt{\overline{v'^2}}$, $-\overline{u'v'}$
	$7.2-32_h$			τ_w, $\sqrt{\overline{\tau'^2}_w}$
	7.0_h	0.125	CF, W	U, V, $\sqrt{\overline{u'^2}}$, $\sqrt{\overline{v'^2}}$, $-\overline{u'v'}$, FV
	$7.5-32_h$			τ_w, $\sqrt{\overline{\tau'^2}_w}$
	7.0_h	0.200	CF, W	U, V, $\sqrt{\overline{u'^2}}$, $\sqrt{\overline{v'^2}}$, $-\overline{u'v'}$
	24_h			P_w
Cary *et al.* (1980)	$22-68_{\Lambda}$	0.010	WT, A	P_w, direct drag, U_i
	$22-68_{\Lambda}$	0.020		
	$22-68_{\Lambda}$	0.040		
Chauve (1981)	$32-115_{\Lambda}$	0.050	T, W	U, V, $\sqrt{\overline{u'^2}}$, $\sqrt{\overline{v'^2}}$, $\sqrt{\overline{w'^2}}$, $-\overline{u'v'}$
Lin *et al.* (1983)	$6.3-13.8_{\Lambda}$	0.010	WT, A	P_w, direct drag
	$12.4-69_{\Lambda}$	0.020		
	$12.4-69_{\Lambda}$	0.030		
	$12.4-69_{\Lambda}$	0.040		
Buckles (1983)	12_h	0.200	CF, W	U, $\sqrt{\overline{u'^2}}$, $S(u)$, $F(u)$, P_w, $\sqrt{\overline{p'^2}_w}$
	12_h	0.125	CF, W	U, $\sqrt{\overline{u'^2}}$, P_w, $\sqrt{\overline{p'^2}_w}$
Abrams (1984)	$6.0-12.3_h$	0.014	CF, W	τ_w, $\sqrt{\overline{\tau'^2}_w}$
Frederick & Hanratty	6.4_h	0.031	CF, W	U, $\sqrt{\overline{u'^2}}$
(1988)	$77.6_{\Lambda}(38.8_h)$	0.050		U
Kuzan (1986)	48_h	0.125	CF, W	U, $\sqrt{\overline{u'^2}}$, $S(u)$, $F(u)$, P_w
	33_h	0.125		U, $\sqrt{\overline{u'^2}}$, $S(u)$, $F(u)$, P_w, FV
	4.1_h	0.200		U, $\sqrt{\overline{u'^2}}$, $S(u)$, $F(u)$, P_w, FV
Hudson *et al.* (1996)	$> 3.4_h$	0.100	CF, W	U, V, $\sqrt{\overline{u'^2}}$, $\sqrt{\overline{v'^2}}$, $-\overline{u'v'}$, P_k, FV
Gong *et al.* (1996),	3.8_{Λ}	0.158	WT, A	U, V, $\sqrt{\overline{u'^2}}$, $\sqrt{\overline{v'^2}}$, $\sqrt{\overline{w'^2}}$,
Miller (1995)				$-\overline{u'w'}$, P_w, τ_w
				Secondary flow observed
Russ & Beer (1997)	$0.3-13_d$	0.106	T, A	FV and heat transfer measurements
Nakagawa *et al.* (2001)	46_h	0.10 (0.1)	CF, W	Turb. quantities, connection to fully rough surface

TABLE 1. Summary of experimental studies. A = Air, CF = Channel flow, T = Tube flow, W = Water, WT = Wind tunnel flow, FV = Flow visualization.

References	Description of Investigation
Benjamin (1958)	ST. Linear disturbance theory.
Bordner (1978)	Nonlinear analysis of laminar flow over wavy boundary.
Markatos (1978)	RANS. Heat and mass transfer across a wavy boundary two equation closure.
Balasubramanian *et al.* (1982)	RANS. Zero and two-equation closures.
Caponi *et al.* (1982)	Simulation of turbulent flow over moving wavy boundary.
Patel *et al.* (1991)	$Re_h = 6400$, $\alpha = 0.3125$ (sep. flow), (ref. measurements by Frederick (1986)), and $Re_h = 4080$, $\alpha = 0.2$. non-separated flow (ref. measurements by Kuzan (1986)) RANS, two-layer k, ϵ-closure.
Krettenauer & Schumann (1991)	DNS and LES simulation of turbulent flow over wavy boundary, transport of passive scalar.
Hino & Okumura (1993)	$Re_h = 3400$, $\alpha = 0.0184$, DNS, quasi-stationary streaky pattern at wavy surface observed.
Wang *et al.* (1997)	Modeling turbulent boundary layer flow over wavy surface (terrain).
Maass & Schumann (1996)	$Re_h = 3380$, $\alpha = 0.1$, $\Lambda/H = 1$, $B/\Lambda = 2$, DNS.
Phillips & Wu (1994), Phillips *et al.* (1996)	ST. Existence of longitudinal vortices in turbulent flow over wavy boundary.
De Angelis *et al.* (1997)	$\alpha = 0.1$, $\Lambda/H = 1.04$, $B/\Lambda = 1$, DNS.
Cherukat *et al.* (1998)	$Re_h = 3460$, $\alpha = 0.1$, $\Lambda/H = 1$, $B/\Lambda = 2$, DNS.
Henn & Sykes (1999)	$Re_h = 6560 - 20060$, $\alpha = 0.031 - 0.2$, $\Lambda/H = 1$, $B/\Lambda = 1$, LES
Boersma (2000)	$Re_h = 1750$, $\alpha = 0.1$, $\Lambda/H = 1$, $B/\Lambda = 3$ DNS of particle-laden flow over waves. Indications for streamwise-oriented structures found.

TABLE 2. Summary of selected theoretical investigations and computer simulations. RANS = Reynolds averaged Navier–Stokes equations, ST = Stability analysis.

wave troughs bounded by the isosurface for vanishing mean streamfunction that is obtained by integrating the mean streamwise velocity in the y-direction:

$$\Psi(x, y) = \frac{\int_{y_w}^{y} U(x, \tilde{y})\, \mathrm{d}\tilde{y}}{U_b 2h}. \tag{4}$$

In the vicinity of the separated region, scalings that are commonly applied to free shear layers were used to describe the flow (Hudson, Dykhno & Hanratty, 1995). At the uphill side of the wave, two regions of maximum positive (II) and negative (III) Reynolds shear stress, $-\varrho\overline{u'v'}$, are found. From the DNS results of Cherukat, Hanratty & McLaughlin (1998) for $Re_h = 3460$, the locations of regions (II) and (III) are approximately 0.08Λ and 0.01Λ above the wall at the uphill side. Furthermore, the data of Cherukat *et al.* (1998) and Henn & Sykes (1999) identify the energy of transverse velocity fluctuations, $\varrho\overline{w'^2}$, to be maximal at a location that is close to region (III).

Flow structure

Longitudinal structures play a dominant role in a number of transport processes, e.g. streaky structures for turbulence generation in the vicinity of a solid wall (Robinson 1991), or Langmuir circulations at gas–liquid interfaces (Craik 1977). Even though such structures are of three-dimensional nature, the mostly qualitative visualizations were restricted to observations in the (x, y)-plane. Only recently, was attention drawn to the effect of the wavy wall on the formation of three-dimensional

large-scale structures. The literature on the stability of a sheared flow over rigid waves suggests different mechanisms to produce, or catalyse, spanwise-periodic longitudinal vortices: the Görtler (Görtler 1940; Saric 1994) and the Craik–Leibovich type-2 (CL2) instability (Phillips & Wu 1994). The work of Phillips & Wu (1994) on the development of longitudinal vortex modes in inviscid linear shear and of Phillips, Wu & Lumley (1996) on the inviscid and viscous instability of power-law and logarithmic velocity profiles to spanwise-periodic longitudinal vortex modes, explain the presence of longitudinal large-scale structures with a CL2 instability. Gong, Taylor & Dörnbrack (1996) and Miller (1995) were the first to show the presence of such structures from single-point measurements in a turbulent BL flow over waves, and to connect them to a CL2 instability. However, the small aspect ratios of the facilities used of approximately 4:1 for both experiments are likely to have affected the lateral motion of the large-scale structures. Most numerical studies were performed for relatively small spanwise domain sizes. For a DNS with a spanwise domain of 3Λ, Boersma (2000) recently obtained indications of such large-scale structures in instantaneous fields of the streamwise velocity in the (y, z)-plane. There is a lack of detailed laboratory or computer experiments on the BL or internal flow over two-dimensional waves with larger spanwise domains to clarify the role and lateral motion of such flow structures. Before characterizing the experimental details of the present work in § 2, we briefly summarize the motivations for previous studies.

Reference flow with separation

The waviness of the bottom wall adds a degree of complexity to the flat-walled channel flow, but the flow conditions remain as they are for the flat-walled channel, well-defined by the no-slip conditions at the channel walls and periodicity (except for the pressure) at the inflow and outflow sections. This is a significant advantage over other test cases for separated flows, namely the flow over a backward or forward facing step (Stüer 1999), where the proper definition of the inflow conditions remains a challenge for laboratory and numerical experiments. Separation occurs behind the wave crests, thus multiple time scales persist. At moderate Reynolds numbers, detailed comparisons with DNS are therefore possible.

Hydrodynamically rough wall

Turbulence production at smooth walls has been widley studied by numerical and experimental means. The formation of streamwise vortices in the wall region has been identified as a key issue in understanding how turbulence is sustained. Altering those structures is seen as an effective tool for changing mean and turbulence properties of the flow, most notably the drag. Turbulence production and sustainment in the near-wall region, and thus the turbulence structure, are likely to be different from a smooth surface. However, a similarity of the structures in the outer flow has been hypothesized by Raupach, Antonia & Rajagopalan (1991). By using wavelengths that are ten times smaller than the channel height and Nakagawa & Hanratty (2001) systematically address this problem for $\alpha = 0.1$ and connect it to a fully rough surface.

Flow over topology and wavy gas–liquid flows

Many technically, geophysically or environmentally relevant flows occur over rough or structured surfaces. To improve existing models of such flows, DNS and large-eddy simulations (LES) of the flow over sinusoidal waves have been conducted, e.g. Dörnbrack, Gerz & Schumann (1993), and Krettenauer & Schumann (1992). Boersma (2000) studied particle-laden flow over waves by means of DNS. The developed flow over solid waves can be related to non-breaking wavy gas–liquid flows. Since the

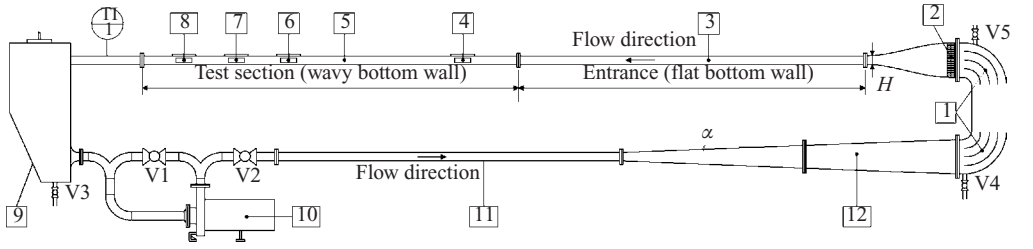

FIGURE 2. Facility with the channel sections and the recirculation system: (1) turning elbows, (2) honeycomb, (3) flat-walled entrance section, (5) section with wavy bottom wall, (4, 6–8) optical view ports, (9) reservoir, (10) frequency-controlled pump, (11) pipe and (12) diffusor.

ratio between the gas and the liquid density is of $O(0.001)$, De Angelis, Lombardi & Banerjee (1997) argue that the gas–liquid flow can be approximated by a fluid flow over a solid wave. Note that the two-dimensional sinusoidal waves considered herein are a simplification of real three-dimensional surface waves. Note also that we consider a standing wavy surface, whereas a moving solid wave would be a closer approximation of a wavy gas–liquid flow.

2. Experiments

Measurements are carried out in a channel facility, see figure 2, with approximately $0.280\,\mathrm{m}^3$ of de-ionized and filtered water as the working fluid. The flow loop is designed for low Reynolds number turbulence measurements with light sheet techniques. The entire facility is made of black anodized aluminium, PVC, and Schott BK-7 glass. All parts are positioned in a welded stainless-steel frame.

Recirculation system

After passing the channel (5 in figure 2), the water flows into a reservoir, (9). A frequency-controlled stainless-steel pump, (10), draws fluid from an intake that is installed at the bottom of the reservoir tank and feeds it through a PVC tube with an inner diameter of 50 mm (10). To reduce transmission of vibrations, the pump has flexible connections at the inflow and the outflow sides. At the outflow side, a 2.25 m long diffusor (12) with a maximum opening angle of 1.9°, (12), is located. Gradual expansion of the inflow tube from the circular cross-section to a rectangular one of 360 mm × 200 mm is done to avoid boundary layer separation, which may affect the flow characteristics in the test section (Niederschulte 1988). The direction of the flow is changed with turning vanes, (1) in figure 2. The diffusor and the section with the turning elbows are made of black anodized aluminium and interconnected through flanges. The flow then passes a honeycomb, (2), with a hexagonal cell structure of carbon-fibre reinforced plastics. A honeycomb length-to-cell-size ratio of seven is used. At the entrance to the rectangular channel, the cross-sectional area is reduced by a factor of 6.7 and a boundary layer trip, which extends 1 mm into the flow from all four walls, is positioned. It ensures fully developed turbulent channel flow by uniformly disturbing the boundary layer of the flow.

Channel

With positioning screws, the two channel sections are aligned horizontally and connected to the stainless-steel frame. The full height of the channel, H, is 30 mm, and its aspect ratio, B/H, is 12 : 1. The inflow section of the channel, (3), is 67 channel

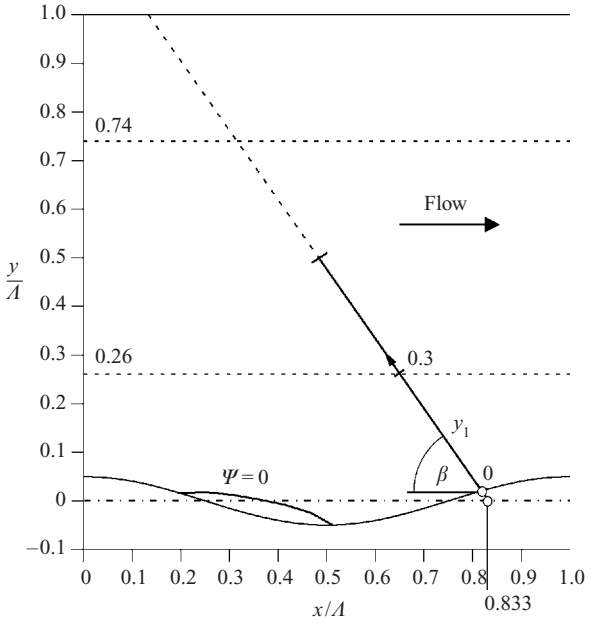

FIGURE 3. Side view of the flow field with the separated region (streamline $\Psi = 0$) and the measurement locations in the (x, z)-plane, and in the (y_1, z)-plane with $\beta = 53°$.

heights long and consists of flat top and bottom walls. Both walls are made of black anodized aluminium with a wall thickness of 6 mm. A second section with a flat top and a wavy PVC bottom wall, (5), has a length of 72 channel heights and offers the possibility of heating the sinusoidal bottom wall resisitively over a section 34 channel heights long. However, all present results are obtained for isothermal flow. Studies on flow over heated waves are reported elsewhere (Günther & Rudolf von Rohr 2002). Positioning screws and liquid sealings at flange connections ensure precise horizontal alignment of both sections. The wavelength Λ of the removable sinusoidal wall profile is equal to the full height of the channel, $H = 2h$, and α is 0.1. A cutting tool with the sinusoidal profile was machined and gauge measurements confirm that the milled PVC wall deviates less than 0.24% from the ideal sinusoidal shape.

Test section

Optical access is provided at four streamwise locations of the wavy channel section through viewing ports (positions 4, 6, 7, 8 in figure 2) at both sidewalls (thickness 5 mm) and at the flat top wall (thickness 7 mm), all flush mounted to the channel inner walls and made of optical grade Schott BK-7 glass. Measurements are performed at the positions (4, developing flow) and (7, developed flow) after the 4th and the 50th wave crest. Side windows provide optical access with a maximum area of view (AOV) of 3Λ(streamwise)$\times 1.2\Lambda$(normal), where the maxiumum AOV for the top windows is 3.3Λ(streamwise)$\times 3.3\Lambda$(spanwise). Figure 3 illustrates the measurement planes in the test section. The Reynolds number is adjusted through the pump frequency and determined by monitoring the flow rate and temperature of the water. In its present configuration, the facility allows measurements between laminar flow conditions and a maximum Reynolds number of approximately 8000.

We use digital particle image velocimetry (PIV) (Westerweel 1993; Adrian 1991) to experimentally assess the role of large-scale structures in the velocity field. The

flow is seeded with monodisperse 30 micron spherical Latex particles (Pharmacia Biotech product Source 30 ETH). The measurement system consisting of the laser, the laser optics, and the camera, is positioned on a traverse that allows the vertical position to be altered. The measurement accuracy of adjusting the y-position with the traverse is approximately 10 microns. A flashlamp-pumped dual Nd : YAG laser ($\lambda = 532\,\mathrm{nm}$, New Wave, Inc., Minilase III) provides the pulse light source and two CCD cameras, a 8 bit Kodak Megaplus ES 1.0 with a spatial resolution of 1008 (horizontal) $\times$ 1016 (vertical) pixels^2, and a 12 bit PCO SensiCam with a spatial resolution of 1280 (horizontal) $\times$ 1024 (vertical) pixels^2 are used for image acquisition. Both are components of a commercial PIV system of TSI. In § 3, we compare the streamwise mean velocity that is obtained from PIV measurements in the (x, y)-plane with literature data and obtain information on how far the longitudinal structures extend in the normal direction away from the surface. In § 4, longitudinal structures are identified based on their instantaneous streamwise velocity in the (x, z)-plane at the vertical distances $y/\Lambda = 0.26$ and 0.74. Since the spanwise extent of the flow domain is large, they are expected to meander laterally. In § 5, a measurement plane that intersects with the wavy surface at the uphill side of the flow, is considered.

3. The smallest resolvable (x, y)-plane

In order to connect to previous work, flow conditions close to those of a laser Doppler velocimetry study by Hudson (1996), and a DNS by Cherukat *et al.* (1998) are chosen. Measurements in the (x, y)-plane are performed at a Reynolds number of 3350, with two AOV, $0.99\Lambda \times 0.79\Lambda$ and $1.1\Lambda \times 1.1\Lambda$. The first allows a more detailed assessment of the separated region in the wave troughs, whereas the latter includes the entire flow field between the wavy bottom and the flat top wall and therefore allows the bulk velocity to be obtained equation (3) and the Reynolds number of the flow. It should however be noted that the large AOV limits the spatial resolution in characteristic regions of the flow, namely in the vicinity of the walls. For the AOV, the smallest resolvable spot was $0.03\Lambda \times 0.03\Lambda$.

3.1. *Instantaneous and mean flow*

For a Reynolds number of 3350, figure 4 provides qualitative information on the structure of the flow in the (x, y)-plane from six instantaneous realizations for the dimensionless velocity fluctuations (outer scales) in the streamwise and normal directions of the mean flow. The Kodak camera is used with the larger AOV. Even though judgement based on instantaneous information is subjective, since nothing is known about the significance of one particular instant in time with regard to the entire flow field, it provides useful information on the scales and complexity of the flow. Consistent with previous findings, large ejections of fluid are observed in the wave trough, which can reach far into the outer flow, almost to the top wall (Hudson 1993). Figure 5 (*a–c*) shows contour plots of the mean streamwise velocity, U/U_b, the mean normal velocity, $V(x, y)/U_b$, and the mean stream function, $\Psi(x, y)$. The averages are obtained from 250 instantaneous velocity fields that were acquired in the frame-straddle mode at a rate of 1 Hz. The PCO Sensicam camera is used with the smaller AOV. Outer scaling is applied for the velocities, i.e. they are made dimensionless with the bulk velocity, $U_b = 0.22\,\mathrm{m\,s^{-1}}$. In figure 6, the streamwise mean velocities that are obtained from PIV measurements in the (x, y)-plane are compared with the laser Doppler velocimetry (LDV) data of Hudson *et al.* (1996). Since Hudson *et al.*'s data were restricted to the lower channel half, the common definition for the bulk

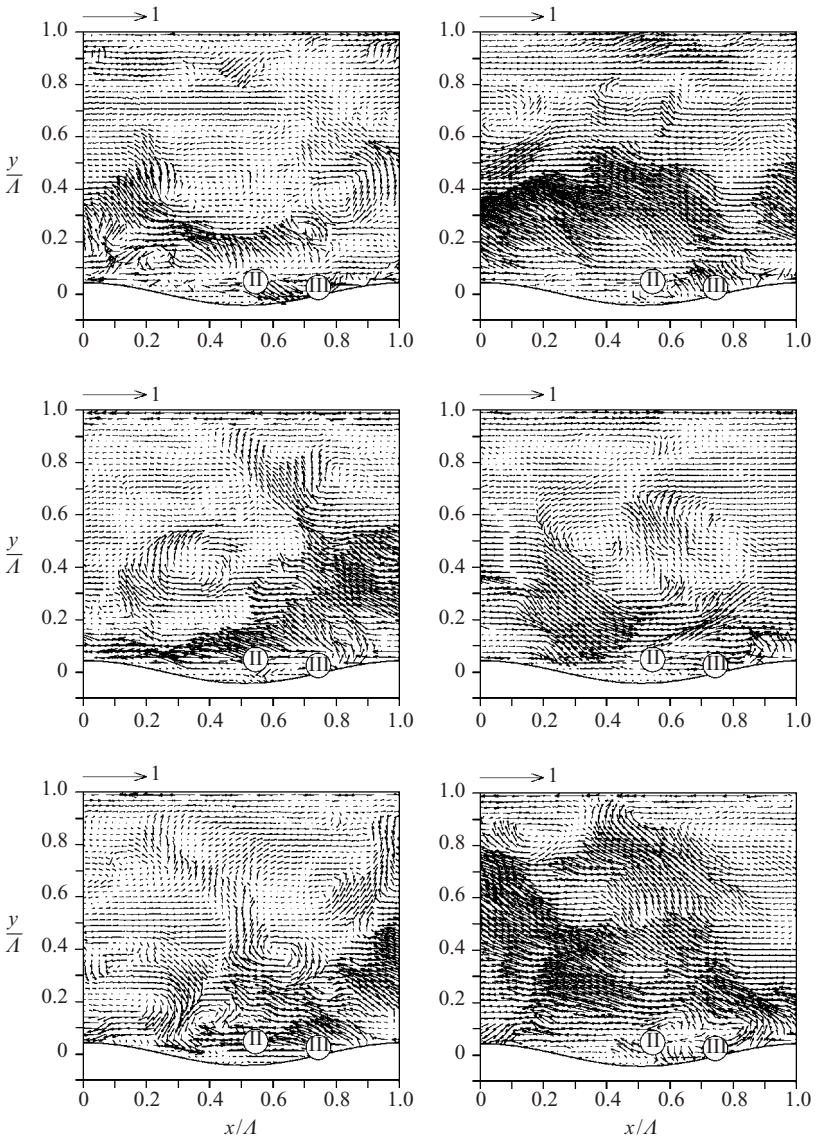

FIGURE 4. Instantaneous velocity fluctuations in the streamwise, u'/U_b (left), and the normal direction, v'/U_b (right), in the (x, y)-plane at $Re_h = 3350$. AOV$= 1.1\Lambda \times 1.1\Lambda$.

velocity, (3), is not applicable. In order to compare the data, our velocities are made dimensionless with the streamwise mean velocity that is obtained from integrating $U(x, y)$ over the lower channel half:

$$U_{b,Hudson} = \frac{1}{h\Lambda} \int_0^{\Lambda} \int_{y_w}^{h} U(x_\xi, y)\, \mathrm{d}y\, \mathrm{d}x. \tag{5}$$

In figure 6, the profiles of the streamwise mean velocity are compared at the two locations, $x/\Lambda = 0.0$ (crest) and $x/\Lambda = 0.5$ (trough). Considering the limited resolution of the PIV measurements of 0.04Λ, a good agreement is obtained. Figure 5(c) shows

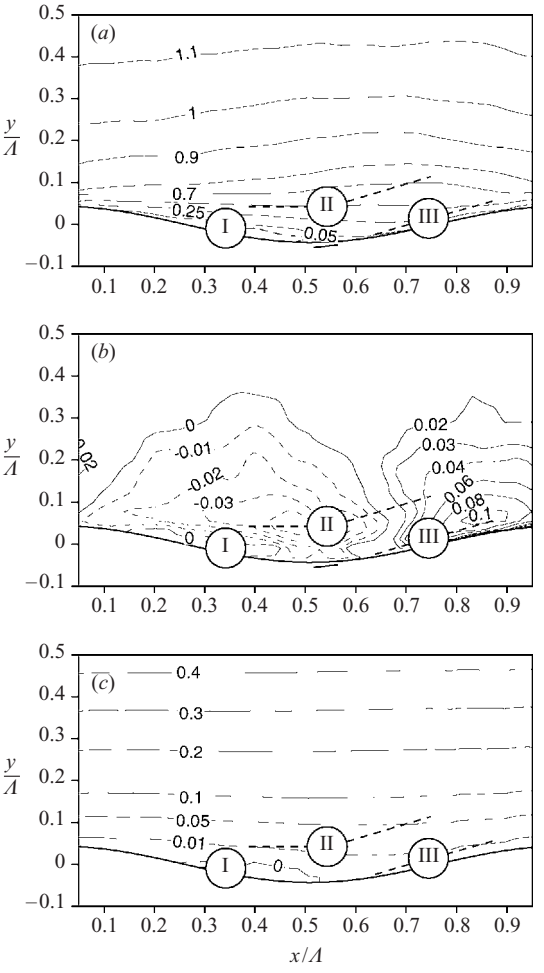

FIGURE 5. Contours of (*a*) the dimensionless mean streamwise velocity, U/U_b, (*b*) the mean spanwise velocity, V/U_b, and (*c*) the mean stream function in the (x, y)-plane in outer scales for the flow over waves at $Re_h = 3350$. Solid lines represent positive and broken lines negative velocities.

the mean stream function at the Reynolds number of 3350. Streamline $\Psi = 0$ bounds the separated region.

Contours of the turbulence intensities in the streamwise and normal directions and the Reynolds shear stress are shown in figure 7. Consistent with the conceptual sketch in figure 1, three distinct regions are found. First, a surface of vanishing Ψ bounds the separated region. The two intersections of that surface with the wavy wall represent the separation and reattachment lines, which are oriented perpendicular to the (x, y)-plane. Note that, in comparison with the instantaneous flow fields in figure 4, the locations of separation and reattachment are not spatially fixed but they change transiently. Secondly, the streamwise turbulence intensity has a maximum at a location above the wave crest that coincides with a maximum of the Reynolds shear stress, region (II). It is consistent with the experimental results of Hudson *et al.* (1996), and with the numerical prediction of Cherukat *et al.* (1998). Third, a region (III) of minimum Reynolds shear stress is located in the vicinity of the wavy wall on

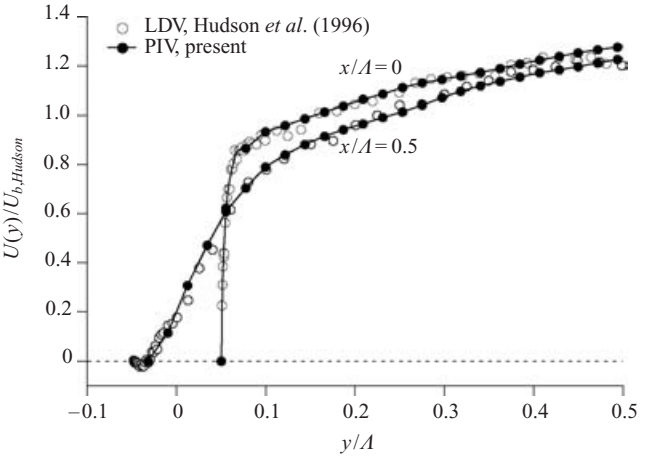

FIGURE 6. Comparison of the dimensionless mean streamwise velocity, $U/U_{b,Hudson}$, at the two locations, $x/\Lambda = 0.0$ (crest) and $x/\Lambda = 0.5$ (trough, separated region) at $Re_h = 3350$ with the LDV data of Hudson *et al.* (1996).

its uphill side. This region has previously been connected to structural information in recent DNS and LES studies (e.g. Henn & Sykes 1999). Note that the limited dynamic and spatial resolution of the PIV measurements limits the accessibility of region (III), see figure 1.

3.2. *POD analysis*

From the PIV measurements in the (x, y)-plane, the streamwise and the normal velocity components, $u(x, y, t)$ and $v(x, y, t)$, are obtained at discrete times t_i, with $i = 1, \ldots, M$, at $1, \ldots, m$ discrete x-locations, and $1, \ldots, n$ discrete locations in the y-direction. To characterize large-scale flow structures at turbulent conditions, we perform a proper orthogonal decomposition (POD) or Karhunen–Loève (KL) decomposition of the stream-wise velocity component (Liu, Adrian & Hanratty 2001; Berkooz, Holmes & Lumley 1993). We use the method of snapshots (Sirovich 1987). A single coordinate $\xi = 1, \ldots, N$ with $N = n\,m$ distinguishes between the different positions in the (x, y)-plane. We write the set of spatio-temporal velocity data as

$$\boldsymbol{U} = \{\boldsymbol{U}_i\}_{i=1}^{M} = \frac{1}{U_b}\begin{bmatrix} u_{11}, u_{11}, \ldots, u_{1M} \\ u_{21}, u_{22}, \ldots, u_{2M} \\ \vdots \\ u_{N1}, u_{N2}, \ldots, u_{NM} \end{bmatrix}, \tag{6}$$

with $\boldsymbol{U}_i = 1/U_b[u_1, u_2, \ldots, u_N]^T$. Note that the $N \times M$-matrix $\boldsymbol{U}$ is already normalized with U_b. We obtain the mean velocity by averaging over the columns:

$$\overline{\boldsymbol{U}} = \frac{1}{M}\sum_{i=1}^{M} \boldsymbol{U}_i, \qquad i = 1, \ldots, M. \tag{7}$$

For the velocity fluctuations then

$$\boldsymbol{U}_i' = \boldsymbol{U}_i - \overline{\boldsymbol{U}}, \qquad i = 1, \ldots, M. \tag{8}$$

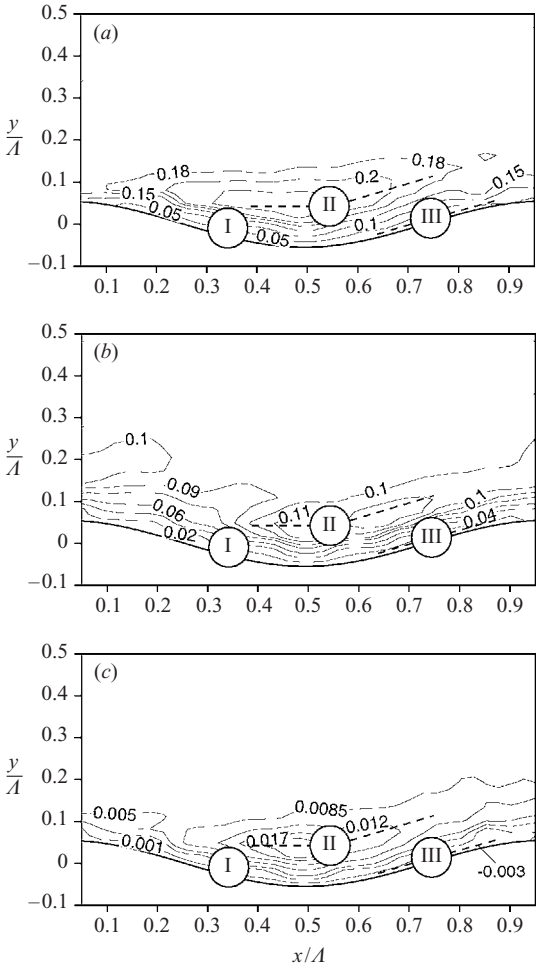

FIGURE 7. Contours of (*a*) the turbulence intensity in the streamwise direction, $\sqrt{u'^2}/U_b$, (*b*) in the normal direction (bottom), $\sqrt{v'^2}/U_b$, and (*c*) the Reynolds shear stress $-u'v'/U_b^2$ in the (x, y)-plane for flow over waves at $Re_h = 3350$.

Using the method of snapshots, the $M \times M$ covariance matrix becomes

$$\boldsymbol{C}_{ij} = \langle \boldsymbol{U}'_i \boldsymbol{U}'_j \rangle, \qquad i, j = 1, \ldots, M, \tag{9}$$

where $\langle \cdot, \cdot \rangle$ is the Euclidean inner product. Since the matrix is symmetric its eigenvalues, λ_i, are non-negative, and its eigenvectors, ϕ_i, $i = 1, \ldots, M$, form a complete orthogonal set. The orthogonal eigenfunctions are:

$$\Pi^{[k]} = \sum_{i=1}^{M} \phi_i^{[k]} \boldsymbol{U}'_i, \qquad k = 1, \ldots, M, \tag{10}$$

where $\phi_i^{[k]}$ is the ith component of the kth eigenvector. Note that index i distinguishes between velocity fields that are taken at different instances in time, not between different velocity components. For the contribution of the streamwise fluctuations to

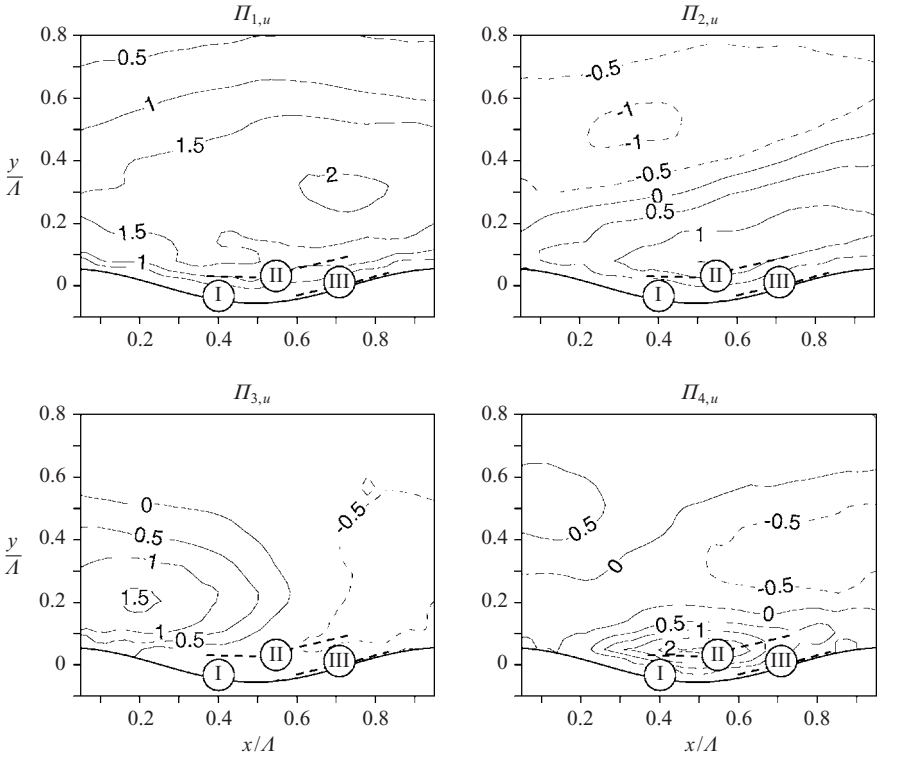

FIGURE 8. Contours of the eigenfunctions $\Pi_{1,u}, \ldots, \Pi_{4,u}$ from for a decomposition of u'/U_b from 250 velocity fields of the developed flow (after the 50th crest) in the (x, y)-plane. Solid lines represent positive and broken lines denote negative values, $Re_h = 3350$.

the turbulence energy we can write

$$E = \left(\frac{u'}{U_b}\right)^2 = \sum_{i=1}^{M} \lambda_i \tag{11}$$

and the fractional contribution of one eigenfunction's associated eigenvalue is

$$\frac{E_k}{E} = \frac{\lambda_k}{E}. \tag{12}$$

Note that both the x- and the y-directions are inhomogeneous. Somewhat similar to the approach chosen by Liu *et al.* (2001), we do not attempt to filter characteristic eddies. Figure 8 shows contours of the eigenfunctions $\Pi_{1,u}, \ldots, \Pi_{4,u}$ that correspond to the four dominant modes, $1, \ldots, 4$, being ranked in decreasing order of their fractional contribution to the turbulent kinetic energy in the streamwise direction, E. In figure 9(*a*) the fractional contributions E_k/E and the cumulative values for $\lambda_1, \ldots, \lambda_{30}$ are shown for a sample size of 250 and $Re_h = 3350$, where λ_1/E already contributes 33% of the kinetic energy of the streamwise velocity fluctuations. In figure 9(*b*), the eigenfunction, $C\Pi_{1,u}(x/\Lambda = 1.0, y)$, is plotted above the crest location $x/\Lambda = 1.0$. The curve is normalized so that its maximum is equal to unity. The data suggest that the dominance of mode 1 is limited to the lower channel half. Since the curve has a pronounced maximum location at $y/\Lambda \approx 0.26$, we will select this plane for our measurements in the (x, z)-plane. Phillips *et al.* (1996) conducted a stability

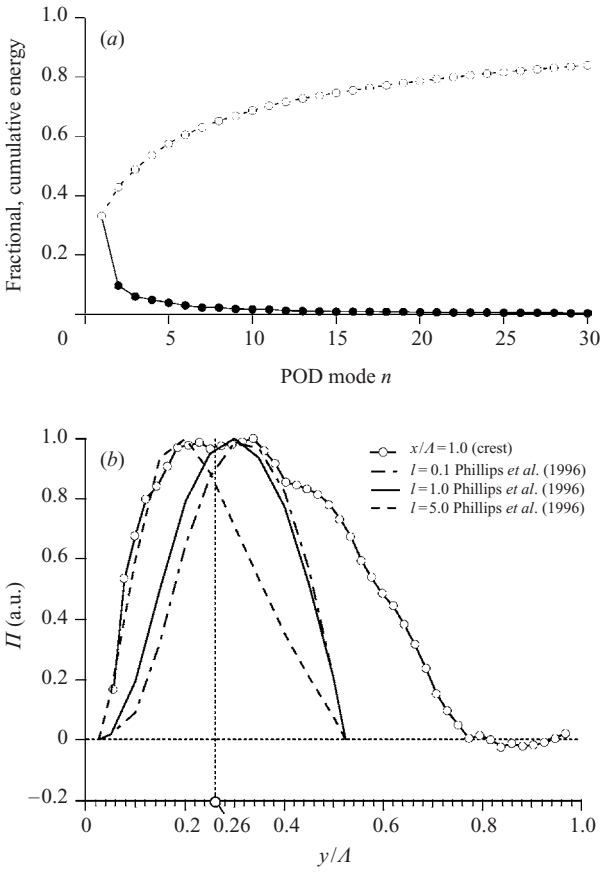

FIGURE 9. (*a*) Fractional energy E_k/E (solid line) of the thirty dominant POD modes and the cumulative energy (broken line) from a decomposition of u'/U_b for the developed flow in the (x, y)-plane at the Reynolds number, $Re_h = 3350$. (*b*) The spanwise variation of the dominant eigenfunction above a crest location, $\Pi_1\,(x/\Lambda = 1.0)$, is compared with the prediction of Phillips *et al.* (1996). Phillips *et al.* approximate a boundary layer flow by a power-law or logarithmic velocity profile ($l = 0.1, 1, 5$ and $2\pi\delta/\Lambda = 1$). Position $y/\Lambda = 0.26$ is where measurements are obtained in the (x, y)-plane.

analysis for a boundary layer flow over waves. They approximated the flow field by a power-law and a logarithmic profile and obtained eigenfunctions of the streamwise velocity in the normal flow direction that are included in the figure. The shape of the eigenfunctions was found to be insensitive to the two approximate velocity profiles the authors considered. The stability analysis was conducted for $2\pi\delta/\Lambda = 1$, where δ is the boundary layer thickness. For the experiments conducted by Gong *et al.* (1996) this parameter is approximately 6 (Phillips *et al.* 1996). If we assume $\delta \approx H/2$, we obtain $2\pi\delta/\Lambda \approx \pi$ for the present case. A second parameter, $l = 2\pi\delta/\Lambda_z$, was introduced. Figure 9(*b*) shows the eigenfunctions for $l = 0.1, 1$ and 5 obtained by Phillips *et al.* (1996). Symbol Λ_z denotes a characteristic spanwise separation of the longitudinal structures. By assuming $\delta \approx H/2$, we obtain $l \approx \pi H/\Lambda_z$. The maximum location of $\Pi_{1,u}(x/\Lambda = 1.0, y)$ lies between the numerical results of Phillips *et al.* (1996) for $l = 1$ and 5, i.e. in good agreement. Compared to the result from the stability analysis for a boundary layer flow, the experimentally obtained curve $\Pi_{1,u}(x/\Lambda = 1.0, y)$ for our

channel flow extends further away from the wavy wall. By examining the (x, z)- and the (y_1, z)-planes, we collect quantitative information on Λ_z and connect longitudinal flow structures to the characteristic region (II).

4. The (x, z)-plane

4.1. *Instantaneous and mean flow*

The instantaneous velocities in the (x, z)-plane are obtained at the wall-normal distance $y/\Lambda = 0.26$, see figure 3. In this plane above the wave crests, the perturbations in the velocity field were found to be the largest and the dominant eigenfunction in the (x, y)-plane showed an extremum. Due to the waviness of the bottom wall, the mean flow is weakly inhomogeneous in the x-direction in this plane, whereas the spanwise direction, z, can be considered homogeneous at the measurement location in the channel centre. Measurements in the (x, z)-plane are expected to reveal information that is related to the spanwise extent of large-scale, longitudinal flow structures. In § 5, these structures are connected to smaller scales that can only be observed at locations closer to the wavy wall surface.

To quantitatively address the role of large scales in the (x, z)-plane, we first consider the flow at $Re_h = 700$. Figure 10 shows a sequence of nine contour plots of the instantaneous streamwise velocity obtained from transient PIV measurements with a time separation of 1 s and a large AOV of $2.23\Lambda \times 1.79\Lambda$ with the PCO camera. The streamwise positions $x/\Lambda = 0.0$, 1.0 denote wave crests, and $x/\Lambda = 0.5$, 1.5 are troughs. Initially, the flow is laminar and large variations of the streamwise velocity are found in the spanwise direction. For qualitative information, the flow was first seeded with reflective flakes. Such tracers are extremely non-spherical (Günther 2001) and, when illuminated in a light sheet, reflect light depending on their orientation in the flow. Large fluid columns, which are separated by a distance $O(1.5\Lambda)$ in the spanwise direction can be observed passing the view port at the top wall. In figure 10(*a–d*), the spanwise position of the fluid columns is fixed. In figure 10(*d–f*), a traverse motion of these columns can be observed. Eventually, transition to turbulence occurs in figure 10(*g–i*). In a further step we examine whether similar structures are present at turbulent flow conditions. The Reynolds number considered is 7300. Figure 11 shows a sequence of nine contours for the instantaneous streamwise velocity that is acquired with the same AOV and the maximum frame rate of the PCO camera in the frame straddle mode, 3.75 Hz. Subsequent realizations are therefore separated by 0.27 s. The existence of large-scale longitudinal structures is already obvious from the instantaneous plots. However, the quantitative contributions of the different scales, and the dominant scale cannot be found by such means. One observation however is that the observed longitudinal structures do not have fixed spanwise locations but meander laterally. Figure 12 shows the spanwise variation of the wave-averaged mean streamwise velocity for $Re_h = 3800$ (dotted line) and 7300 (dashed line). The averages are obtained from sequences of 250 vector fields that were acquired with a frame rate of 1 Hz. The curves are made dimensionless with their averages in the spanwise direction

$$\langle U \rangle_{xz} = \frac{1}{\Delta z \Lambda} \int_0^{\Lambda} \int_{z_1}^{z_2} U(z)\, \mathrm{d}z\, \mathrm{d}x. \tag{13}$$

For the two turbulent flow cases, the spanwise variation of the mean streamwise velocity is smaller than $\pm 2\%$. In this context we relate the large spanwise variation of the mean streamwise velocity of up to $\pm 7\%$ that was reported from the wind-tunnel

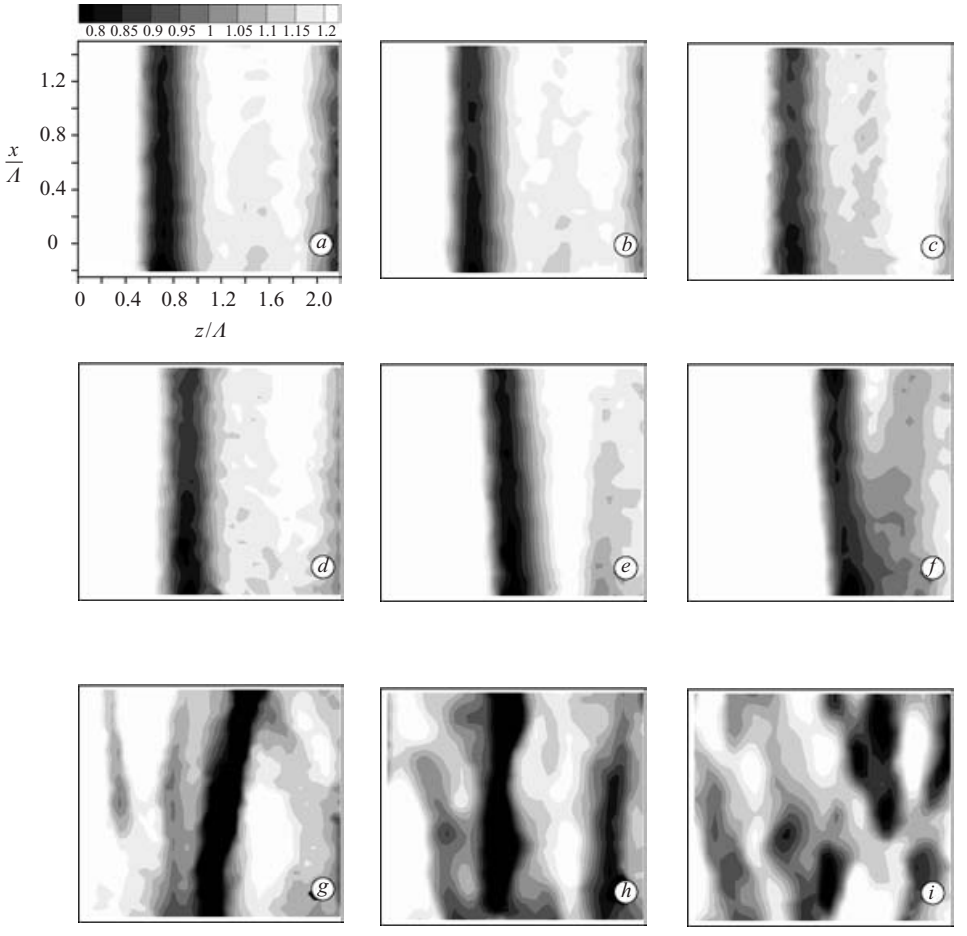

FIGURE 10. Sequence of contours for the instantaneous streamwise velocity, u'/U_b, in the (x, z)-plane at $y/\Lambda = 0.26$ during transition to turbulence at $Re_h = 700$. Streamwise locations $x/\Lambda = 0$, 1.0 denote wave crests, and $x/\Lambda = 0.5$, 1.5 are troughs. The individual velocity fields (*a–i*) are separated by a temporal difference of 1.0 s. AOV $= 2.23\Lambda \times 1.79\Lambda$.

measurements of Gong *et al.* (1996) to the relatively low aspect ratio of their facility. The graph that corresponds to figure 10(*a*) is plotted as a solid line, where spanwise variations of up to $\pm 20\%$ are found.

4.2. *POD analysis*

Since mean quantities do not reveal structural information in the homogeneous z-direction, we conduct a POD analysis from PIV velocity fields in the (x, z)-plane. The streamwise velocity component, $u(x, z, t)$, is given at discrete times t_i, with $i = 1, \ldots, M$, at $1, \ldots, m$ discrete x-locations, and $1, \ldots, n$ discrete z-locations. We use the method of snapshots to conduct a POD analysis in the (x, z)-plane as described in the previous section for the (x, y)-plane.

Since the spanwise flow direction is homogeneous, the POD analysis is identical to a Fourier decomposition in this direction. However, this is not true in the weakly inhomogeneous x-direction, where POD analysis is the correct way of decomposing the velocity field. Figure 13 shows the eigenfunctions $\Pi_{1,u}, \ldots, \Pi_{6,u}$ that correspond to

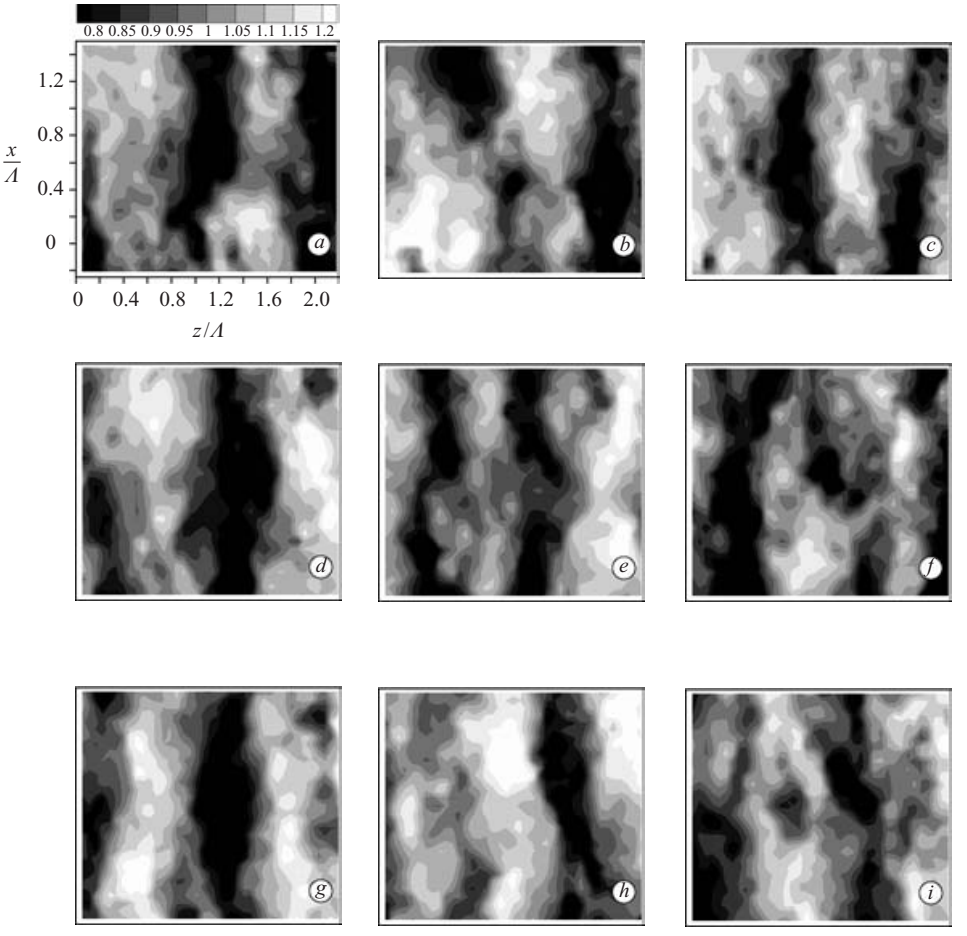

FIGURE 11. Sequence of contours for the instantaneous streamwise velocity, u'/U_b, in the (x, z)-plane at $y/\Lambda = 0.26$. The streamwise locations $x/\Lambda = 0$, 1.0 denote wave crests, and $x/\Lambda = 0.5$, 1.5 are troughs. The individual velocity fields (*a–i*) are separated by a temporal difference of 0.27 s. AOV $= 2.23\Lambda \times 1.79\Lambda$, $Re_h = 7300$.

the six dominant modes, $1, \ldots, 6$, being ranked in decreasing order of their fractional contribution to the turbulent kinetic energy in the streamwise direction, E. Figure 14 shows contours of the fractional contributions E_k/E and the cumulative values for $\lambda_1, \ldots, \lambda_{30}$. Solid circles correspond to $Re_h = 7300$ and open circles to $Re_h = 3800$. The results suggest that, for the Reynolds numbers considered, eigenfunctions $\Pi_{1,u}$ and $\Pi_{2,u}$ have a characteristic scale $\Lambda_z = O(1.5\Lambda)$ in the spanwise direction. This value is identical to the scale that we previously obtained for the spanwise variation of the mean streamwise velocity at laminar conditions. The cumulative contribution of $(E_1 + E_2)/E$ at $Re_h = 7300$ is 31% for the lower and 47% for the higher Reynolds number and therefore increases with increasing Reynolds number. POD modes $1, \ldots, 6$ have cumulative contributions of 55% and 72% respectively. The open triangles in figure 14 show the corresponding curves that are obtained in an (x, z)-plane that is separated from the top wall by the same distance as the two other measurement locations are from the bottom wall, $\Delta y/\Lambda = 0.26$. The Reynolds number is 3800. Comparing the two curves for $Re_h = 3800$ suggests that – in agreement with

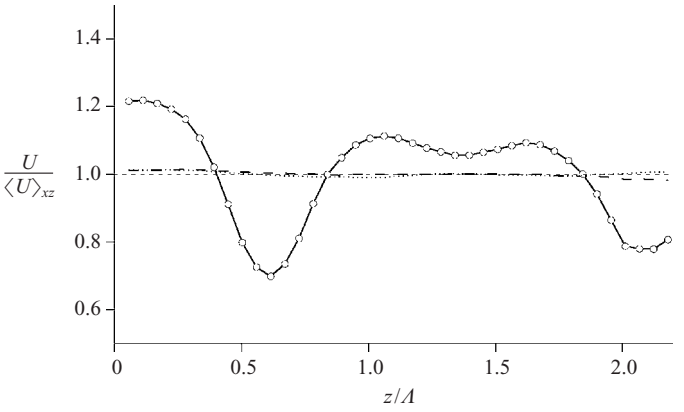

FIGURE 12. Spanwise variation of the streamwise-averaged streamwise mean velocity (normalized) for the turbulent Reynolds numbers $Re_h = 3800$ (dotted line), 7300 (broken line), and for $Re_h = 700$ (solid line with circles) before the transition to turbulence.

the previously presented findings for the (x, y)-plane – the dominance of modes 1 and 2 is limited to the lower channel half.

In the upper half of figure 15, the spanwise variation of the streamwise-averaged eigenfunctions $\langle \Pi_{1,u}(z)\rangle_x$ and $\langle \Pi_{2,u}(z)\rangle_x$ at $Re_h = 7300$ (figure 13) are compared. To allow a comparison, the curves are shifted in the homogeneous spanwise direction so that their maxima coincide at $z/\Lambda = 0$. In the lower half of figure 15, the streamwise-averaged streamwise mean velocity at $Re_h = 700$ before the transition to turbulence occurs is plotted. The mean streamwise velocities obtained by Gong *et al.* (1996) $y/\Lambda = 0.16$ above the 12th crest and by Miller (1995) above the crest of the 9th wave in BL flows are included in the plot. Again, the transverse positions of both curves are adjusted. In the studies of Gong *et al.* (1996) and Miller (1995), wind tunnels with the relatively low aspect ratio of 4 : 1 were used. The comparison between the curves that were obtained at different flow configurations confirm the scale $\Lambda_z = O(1.5\Lambda)$. In that context we note that for the measurements of Gong *et al.* (1996), the spanwise variation of the mean flow was not symmetric about the channel centre, suggesting that Λ_z is not a multiple of Λ. We can summarize that the dominant eigenfunctions suggest a characteristic scale, here $O(1.5\Lambda)$. Their influence is restricted to the lower half of the channel and increases with increasing Reynolds number.

5. The (y_1, z)-plane

In this section we connect the structural information that we obtained in the (x, z)-plane at $y/\Lambda = 0.26$ to structures in the vicinity of the uphill side of the wavy surface. Since the possibilities for laser-sheet measurements in the (y, z)-plane are limited in a water channel facility, we instead consider a plane that is tilted by an angle of $\beta = 53^\circ$ to the x-axis, and refer to it as the (y_1, z)-plane, see figure 3. This plane intersects with the wavy wall at an uphill location, where we expect structural information that is connected to the local curvature of the wall – i.e. the Görtler mechanism (Saric 1994) – and to the Reynolds shear stress maximum, region (II) in figure 1. To obtain distortion-free imaging through the optical view port at the top wall of the channel, we position a second window parallel to the light sheet plane and fill the volume

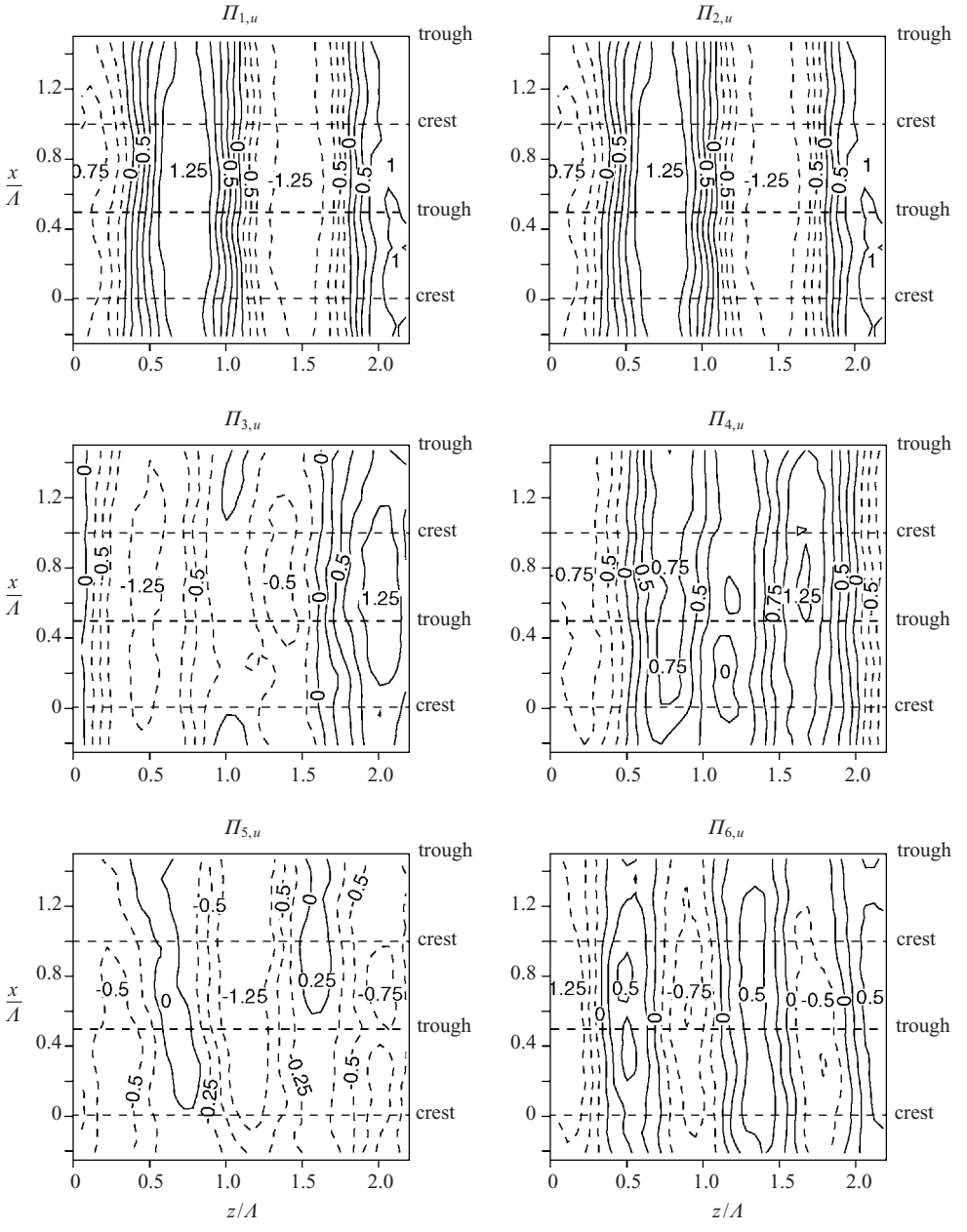

FIGURE 13. Eigenfunctions $\Pi_{1,u}, \ldots, \Pi_{6,u}$ in the (x, z)-plane at $y/\Lambda = 0.26$ from a POD analysis of the streamwise velocity component, u'/U_b. AOV $= 2.23\Lambda \times 1.79\Lambda$, $Re_h = 7300$.

between the two glass windows with water, see figure 16. Such a configuration is sometimes referred to as a water prism.

5.1. *Instantaneous and mean flow*

PIV measurements in the (y_1, z)-plane are challenging since the mean flow passes through the measurement plane, and velocities in the spanwise direction are expected

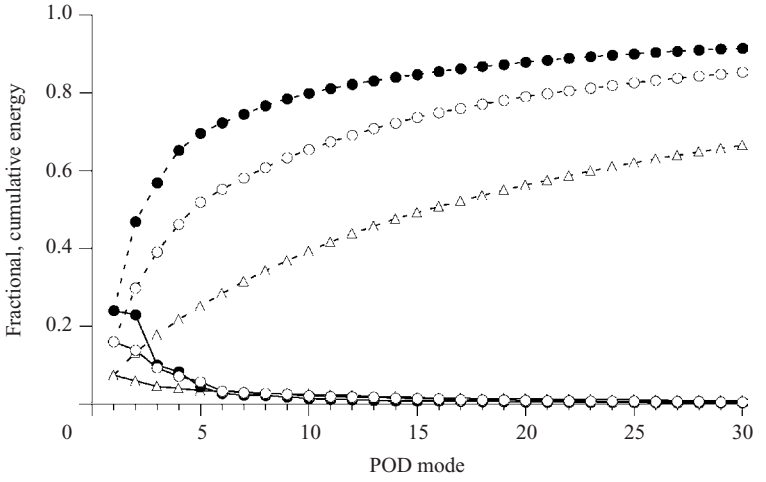

FIGURE 14. Fractional energy E_k/E (solid lines) of the dominant modes $\lambda_1, \ldots, \lambda_{30}$ and cumulative value (broken lines) from a decomposition of u'/U_b for the developed flow in the (x, z)-plane $y/\Lambda = 0.26$ at the two Reynolds numbers, $Re_h = 3800$ (○), and 7300 (●). Curve △ shows the corresponding decomposition of the vector fields that is obtained for the same distance from the flat top wall, $Re_h = 3800$, AOV $= 2.23\Lambda \times 1.79\Lambda$.

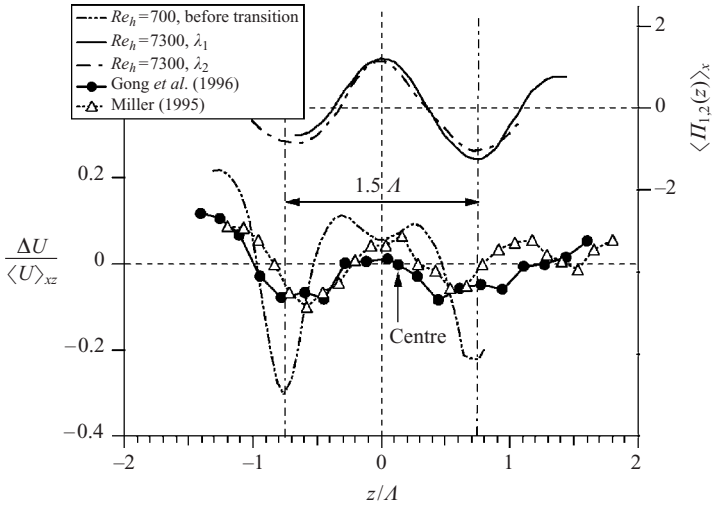

FIGURE 15. Comparison between the spanwise variation of the streamwise-averaged eigenfunctions $\langle \Pi_1(z) \rangle_x$ and $\langle \Pi_2(z) \rangle_x$ at $Re_h = 7300$ (top curves), the streamwise-averaged streamwise mean velocity (normalized) for $Re_h = 700$ before the transition to turbulence. The variation of the mean streamwise velocity Gong *et al.* (1996) (above the 12th crest) and Miller (1995) reported from boundary layer flow measurements are included. Both profiles were obtained for $B/\Lambda \doteq 4:1$ at positions $y/\Lambda = 0.16$.

to be small compared with the mean streamwise velocity. Measurements are performed with the Kodak Megaplus camera. In order to provide an acceptable spatial resolution in the near-wall region, a smaller AOV of $0.67\Lambda \times 0.67\Lambda$ is used. We first examine the flow at laminar conditions. For a Reynolds number of 600, corresponding to a bulk velocity of $0.033\,\mathrm{m\,s^{-1}}$, figure 17 shows the velocity variation in the

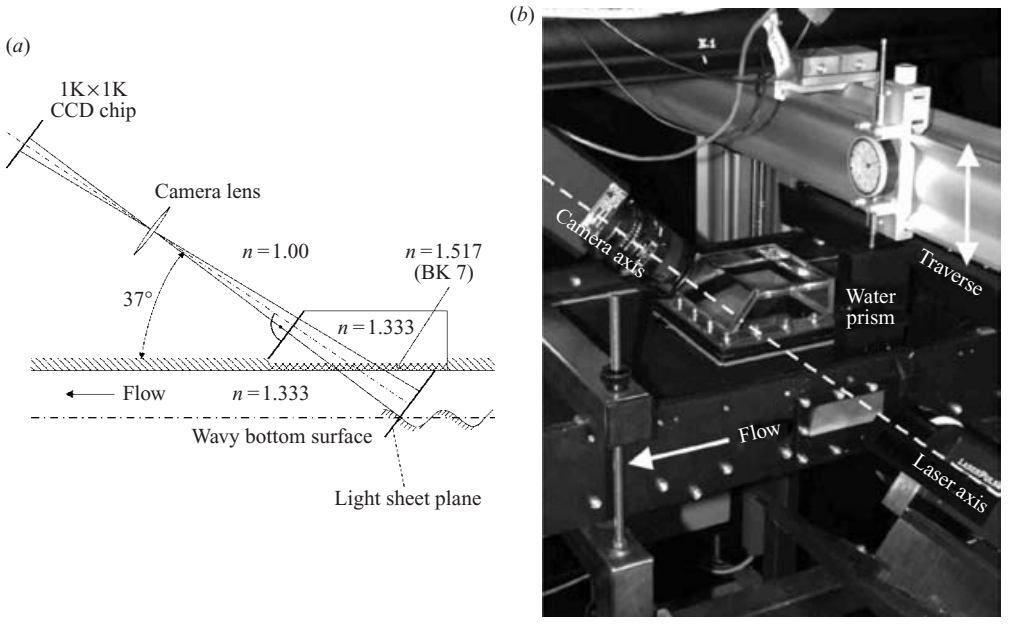

FIGURE 16. Optical configuration for measurements in the (y_1, z)-plane. (*a*) Schematic of the optical path; (*b*) photograph of the set-up with the water prism.

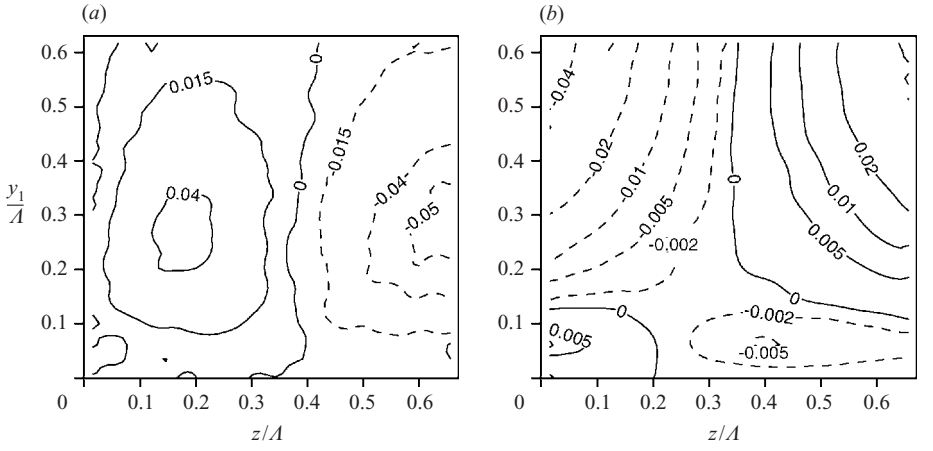

FIGURE 17. Contours of the mean velocities $(V_1 - \langle V_1 \rangle)/U_b$ (*a*) and W/U_b (*b*) for the laminar flow at $Re_h = 600$ in the (y_1, z)-plane. AOV $= 0.67\Lambda \times 0.67\Lambda$.

y_1-direction, $(V_1 - \langle V_1 \rangle_z)/U_b$, and in the spanwise direction, W/U_b, where $\langle V_1 \rangle_z$ denotes an average in the spanwise direction (constant y_1). Line $y_1 = 0$ describes the intersection between the measurement plane and the uphill side of the wall ($x = 0.818\Lambda$, $y = 0.021\Lambda$) and $y_1 = 0.67\Lambda$ corresponds to a location close to the channel centre, ($x = 0.415\Lambda$, $y = 0.556\Lambda$). The (x, z)-plane with $y/\Lambda = 0.26$ that was studied in the previous section intersects the (y_1, z)-plane at $y_1 = 0.30\Lambda$. At turbulent flow conditions, figure 18 shows instantaneous vector fields of the velocities (*a*) and

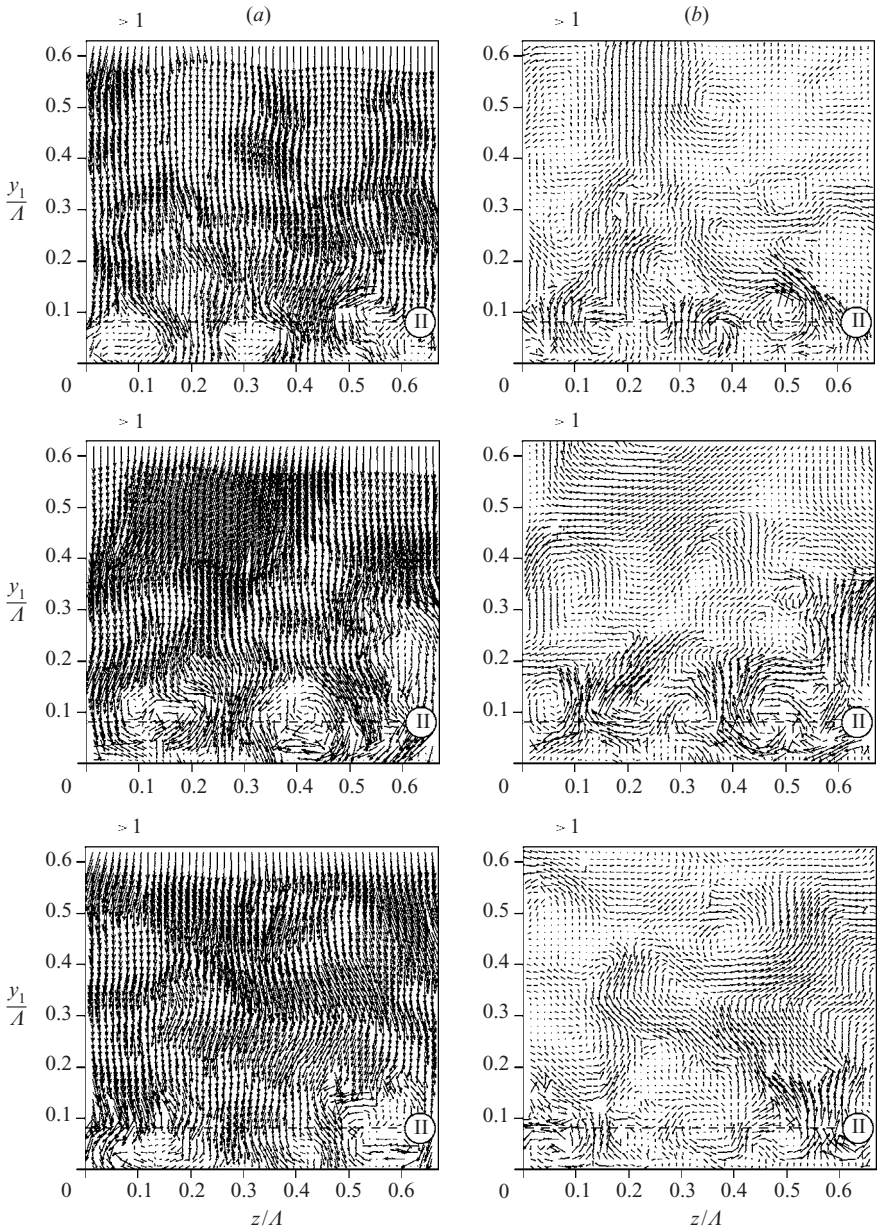

FIGURE 18. Instantaneous velocities (a) and velocity fluctuations (b) in the (y_1, z)-plane. The horizontal broken line marks region (II), where the Reynolds shear stress has a maximum. AOV $= 0.67\Lambda \times 0.67\Lambda$, $Re_h = 3800$.

the corresponding velocity fluctuations (b) that are obtained in the (y_1, z)-plane at three instances in time. The Reynolds number is 3800, and velocities are made dimensionless with the corresponding bulk velocity, $U_b = 0.26\,\mathrm{m\,s^{-1}}$. The broken horizontal line marks region (II) in figure 1, where the Reynolds shear stress has a local maximum. The vortical structures that are found in the instantaneous velocities are located close to region (II).

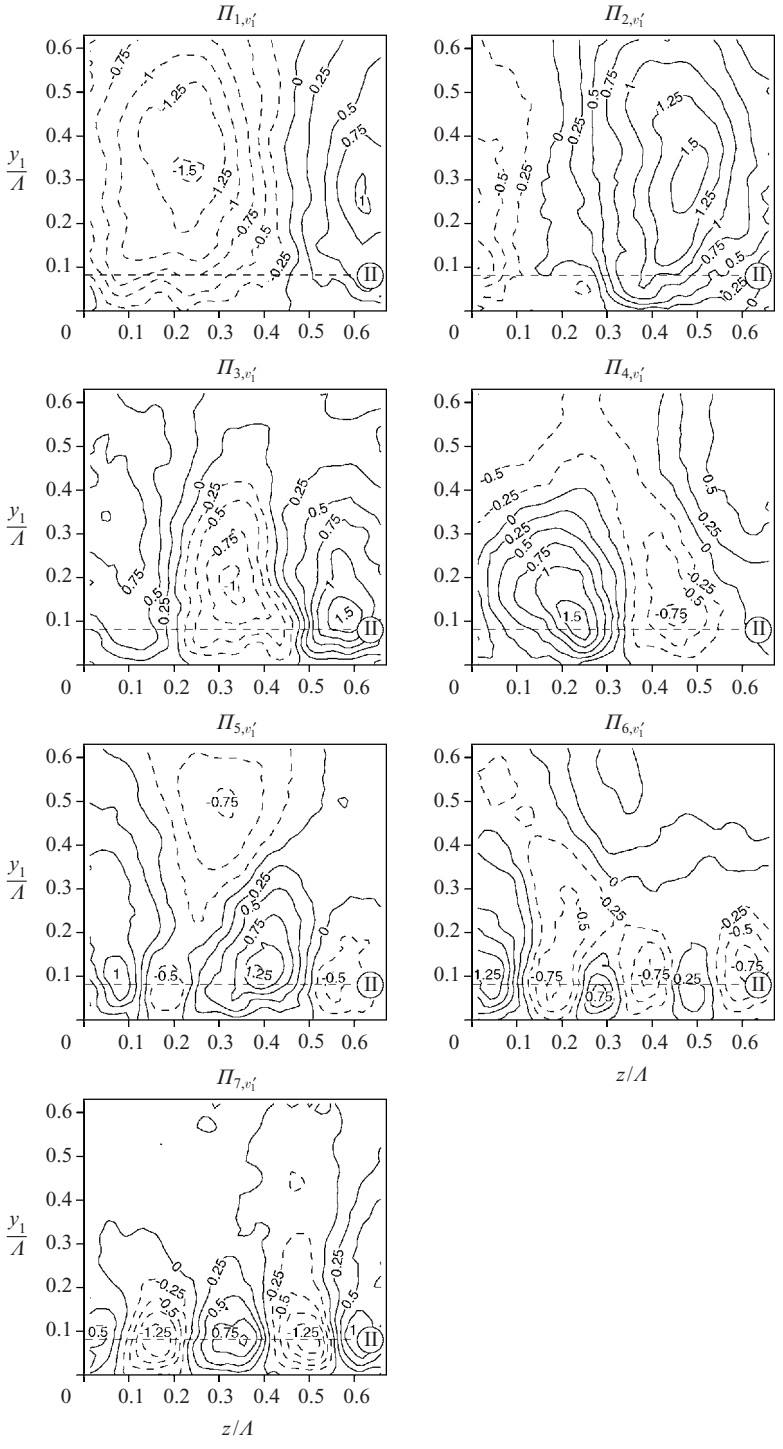

FIGURE 19. Contours of the eigenfunctions $\Pi_{1,v_1'}, \ldots, \Pi_{7,v_1'}$ from the dominant modes $\lambda_1, \ldots, \lambda_7$ for a decomposition of v_1'/U_b from 189 velocity fields of the developed flow (after the 50th crest) in the (y_1, z)-plane. Continuous lines represent positive, broken lines negative values, and the horizontal broken line marks region (II), where the Reynolds shear stress has a maximum. AOV $= 0.67\Lambda \times 0.67\Lambda$, $Re_h = 3800$.

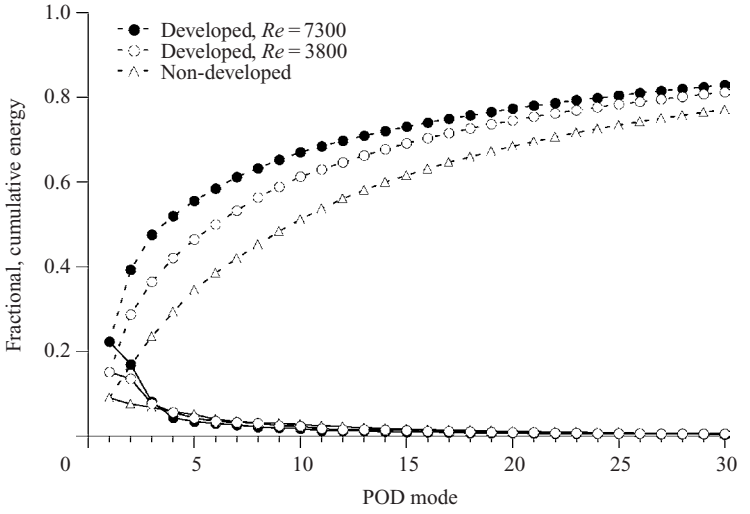

FIGURE 20. Fractional energy E_k/E (dotted lines) of the dominant modes $\lambda_1, \ldots, \lambda_{30}$, and cumulative value (solid lines) from a decomposition of the velocity component v_1/U_b for the developed flow in the (y_1, z)-plane at the two Reynolds numbers, $Re_h = 3800$ (○), and 7300 (●), and for the non-developed flow at $Re_h = 3800$ (△).

5.2. *POD analysis*

To address the contribution of different scales to the energy of velocity fluctuations in the y_1-direction, we perform – as we did in the previous two sections – a POD analysis. Similar to (6), we now consider a set

$$\boldsymbol{V}_1 = \{\boldsymbol{V}_1\}_{i=1}^{M}. \tag{14}$$

A POD analysis is performed for a set of 189 velocity fluctuations

$$\boldsymbol{V}'_{1i} = \boldsymbol{V}_{1i} - \overline{\boldsymbol{V}}_1, \qquad i = 1, \ldots, M, \tag{15}$$

with the mean

$$\overline{\boldsymbol{V}}_1 = \frac{1}{M}\sum_{i=1}^{M} \boldsymbol{V}_{1i}. \tag{16}$$

The frame rate is 1 Hz. Figure 19 shows contour plots of the eigenfunctions $\Pi_{1,v'_1}, \ldots, \Pi_{7,v'_1}$ that correspond to eigenvalues $\lambda_1, \ldots, \lambda_7$. The POD modes are ranked in decreasing order of their individual contribution to the kinetic energy, $E_k = (v'_1/U_b)^2 = \sum_{i=1}^{M} \lambda_i$. The characteristic length scale in the spanwise direction, $O(1.5\Lambda)$ can be connected to the measurements in the (x, z)-plane for the dominant two POD modes. Maxima/minima of $\Pi_{1,v'_1}, \Pi_{2,v'_1}$ are obtained at a wall distance $y_1 \doteq 0.3\Lambda$, corresponding to the location $y = 0.26\Lambda$, where measurements were taken in the (x, z)-plane. Eigenfunctions of higher modes are characterized by smaller Λ_z, 0.2Λ–0.3Λ for POD modes 6 and 7. For these two modes representing the vortical structures we observed in figure 18, we note that the maxima/minima locations of the eigenfunctions coincide with the Reynolds shear stress maximum. Figure 20 shows the fractional (broken line) and cumulative (solid line) contributions to the turbulent kinetic energy amongst the dominant modes, $1, \ldots, 30$. The distribution is plotted for the two turbulent Reynolds numbers, 3800 (open circles), and 7300 (solid circles). Consistent with our findings in the (x, z)-plane, the relative contribution of

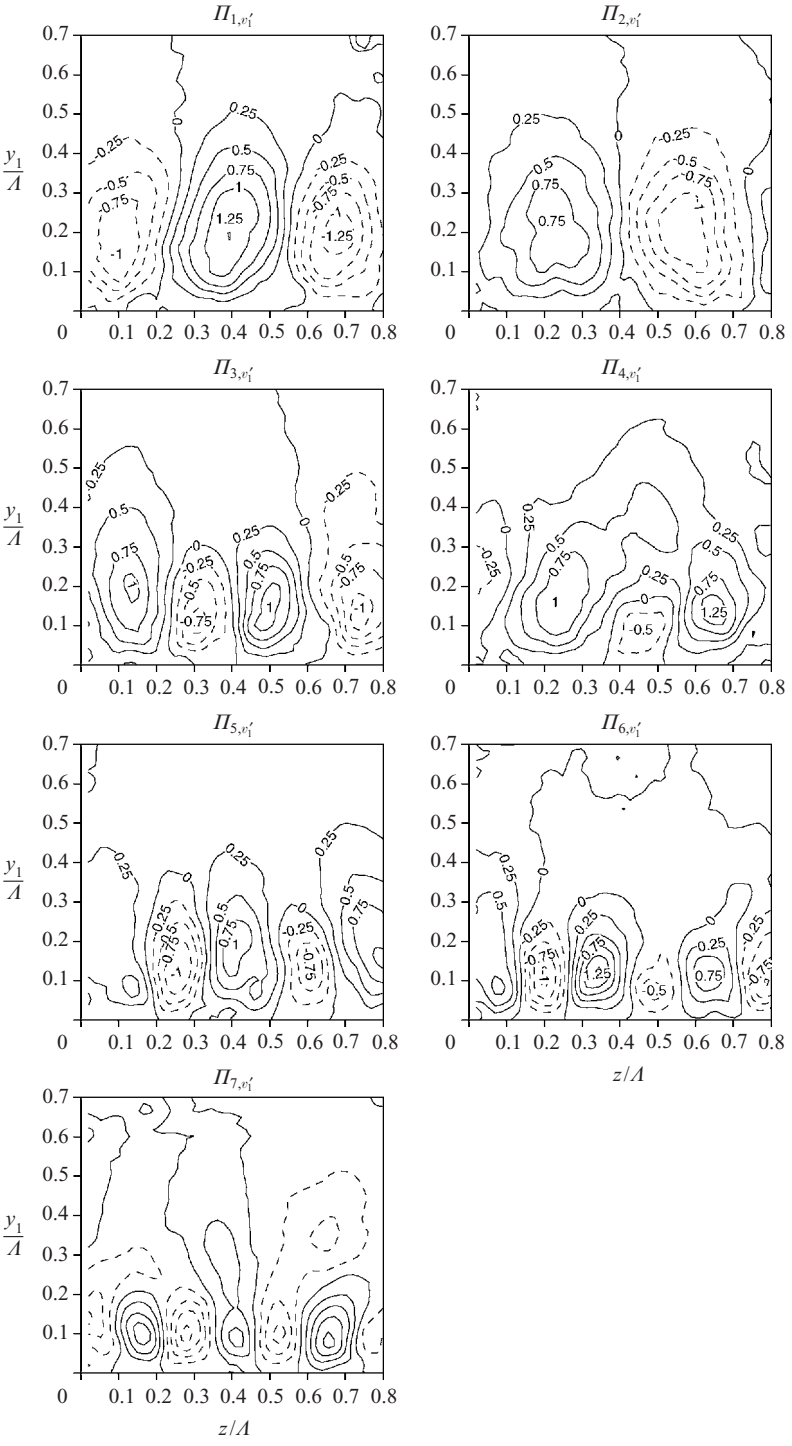

FIGURE 21. Contours of the eigenfunctions $\Pi_{1,v_1'}, \ldots, \Pi_{7,v_1'}$ from the dominant modes $\lambda_1, \ldots, \lambda_7$ for a decomposition of v_1'/U_b from 214 velocity fields of the non-developed flow (after the 4th crest) in the (y_1, z)-plane. Continuous lines represent positive, broken lines negative values. AOV $= 0.82\Lambda \times 0.82\Lambda$, $Re_h = 3800$.

the two dominant modes increases with increasing Reynolds number. For $Re_h = 3800$ and 7300, the cumulative contribution of these modes is 29% and 39%, whereas modes 4–7 contribute 50% and 61% resectively. The triangles show the situation at measurement location (4) in figure 2, where the the non-developed flow is studied at $Re_h = 3800$ in the (y_1, z)-plane after the 4th crest. A comparison with the results for the developed flow shows that a dominance of eigenvalues λ_1, λ_2 is not found. Figure 21 shows the eigenfunctions $\Pi_{1,v_1'}, \ldots, \Pi_{7,v_1'}$ for the non-developed case. Characteristic scales that are obtained from the eigenfunctions of the first modes are smaller than $\Lambda_z = O(1.5\Lambda)$, which was observed for the developed flow. Extrema of the eigenfunctions are located closer to the wavy surface. From these observations we conclude that the non-developed flow does not contain the structures we observe for the developed flow situation, but they develop and grow when passing the periodic train of waves in the streamwise direction.

6. Summary

Based on spatially resolved measurements, we reported on the structure of the developed flow between a wavy bottom and a flat top wall in a water channel facility of aspect ratio 12 : 1. Conditions between laminar flow and turbulent flow at Reynolds number of 7300 are considered. Three characteristic regions of the flow that were previously identified were confirmed from PIV measurements in the (x, y)-plane. To the authors' knowledge, longitudinal structures with a charcteristic scale $\Lambda_z = O(1.5\Lambda)$ in the spanwise direction have been identified for the first time from spatially resolving measurements in the (x, z)-plane at both laminar and turbulent flow conditions ($Re_h = 3800$, 7300). For laminar flow, the observed structures have spatially fixed positions and Λ_z is obtained from instantaneous images. At turbulent flow conditions, proper orthogonal decomposition is used to extract Λ_z from the dominant modes. We find the two dominant modes to contribute almost 50% of the energy contained in the streamwise velocity fluctuations. Considering the spanwise domain sizes of the present DNS and LES studies, the large Λ_z is seen to have considerable implications for computational studies, since it imposes requirements on the spanwise domain size required to accurately resolve all scales of the flow. The value obtained is consistent with the spanwise variation of the streamwise mean velocity reported by Gong *et al.* (1996). In the (y_1, z)-plane an experimental set-up with a water prism enabled us, for the first time, to quantitatively connect the $O(1.5\Lambda)$-structures to those in the vicinity of the wall surface. Based on instantaneous realizations from numerical studies, first evidence of such structures has been supplied by a number of investigators. However, to date, none of those works quantitatively assessed their spanwise extent and energy content. A POD analysis of the v_1-velocity in the (y_1, z)-plane reveals the eigenfunctions of the dominant POD modes 1 and 2 with a characteristic scale $O(1.5\Lambda)$, that were already identified in the (x, y)-plane. The eigenfunctions of modes $4, \ldots, 7$ characterize smaller structures that show local maxima/minima in region (II), the maximum Reynolds stress location.

A. G. wishes to express his sincere gratitude for the support of and many fruitful discussions with Professor Thomas J. Hanratty. Our work has profited from discussions with Professors Leonhard Kleiser, Yang Na, Dimitrios V. Papavassiliou, Thomas Rösgen, and Jerry Westerweel. Dr Werner Dörfler, the workshop of the Institute of Process Engineering, and Mr Bührer of Foba are thanked for their

contributions to the facility. We wish to thank Stefan Fischer for his involvement in this research project. Measurement technology is partially provided by TSI.

REFERENCES

Abrams, J. 1984 Turbulent flow over small amplitude solid waves. PhD thesis, University of Illinois, Urbana.

Adrian, R. J. 1991 Particle-imaging techniques for experimental fluid mechanics. *Annu. Rev. Fluid Mech.* **23**, 261–304.

Balasubramanian, R. & Orszag, S. A. 1982 Numerical studies of laminar and turbulent drag reduction. *NASA CR* 3498.

Beebe, P. S. 1972 Turbulent flow over a wavy boundary. PhD thesis, Colorado State University, Fort Collins.

Benjamin, B. 1958 Shearing flow over wavy boundary. *J. Fluid Mech.* **6**, 161–205.

Berkooz, G., Holmes, P. & Lumley, J. L. 1993 The proper orthogonal decomposition in the analysis of turbulent flows. *Annu. Rev. Fluid Mech.* **25**, 539–575.

Boersma, B. J. 2000 Particle distributions in the flow over a wavy wall. *Proc. Summer School*. Center for Turbulence Res. (CTR), Stanford University.

Bordner, G. L. 1978 Nonlinear analysis of laminar boundary-layer flow over a periodic wavy surface. *Phys. Fluids* **21**, 1471–1474.

Buckles, J. 1983 Turbulent separated flow over wavy surfaces. PhD thesis, University of Illinois, Urbana.

Buckles, J., Hanratty, T. J. & Adrian, R. J. 1984 Turbulent flow over large-amplitude wavy surfaces. *J. Fluid Mech.* **140**, 27–44.

Caponi, E., Fornberg, B., Knight, D., McLean, J., Saffman, P. G. & Yuen, H. 1982 Calculations of laminar viscous flow over a moving wavy surface. *J. Fluid Mech.* **124**, 347–362.

Cary, A. M. Jr, Weinstein, L. M. & Bushnell, D. M. 1980 Drag reduction characteristics of small amplitude rigid surface waves. In *Viscous Flow Drag Reduction* (ed. G. R. Hough), pp. 144–167. AIAA.

Chauve, M. P. 1981 Etude expérimentale d'un ćoulement turbulent en conduite axisymétrique à paroi poreuse ondulée. PhD thesis, University of Aix-Marseille, Marseille.

Cherukat, P., Na, Y., Hanratty, T. J. & McLaughlin, J. B. 1998 Direct numerical simulation of a fully developed turbulent flow over a wavy wall. *Theor. Comput. Fluid Dyn.* **11**, 109–134.

Craik, A. D. D. 1977 The generation of Langmuir circulations by an instability mechanism. *J. Fluid Mech.* **81**, 209–223.

De Agnelis, V., Lombardi, P. & Banerjee, S. 1997 Direct numerical simulation of turbulent flow over a wavy wall. *Phys. Fluids* **9**, 2429–2442.

Dörnbrack, A., Gerz, T. & Schumann, U. 1993 Numerical simulation of turbulent convective flow over wavy terrain. *Boundary Layer Met.* **65**, 323–355.

Frederick, K. A. & Hanratty, T. J. 1988 Velocity measurements for a turbulent nonseparated flow over solid waves. *Exps. Fluids* **6**, 477–486.

Gong, W., Taylor, P. A. & Dörnbrack, A. 1996 Turbulent boundary-layer flow over fixed aerodynamically rough two-dimensional sinusoidal waves. *J. Fluid Mech.* **312**, 1–37.

Görtler, H. 1940 Über eine dreidimensionale Instabilität laminarer Grenzschichten an konkaven Wänden. *Nachr. Ges. Wiss. Göttingen, Math-Phys. Klasse, Neue Folge I*, **2**, 1–26.

Günther, A. 2001 Large-scale structures in Rayleigh–Bénard convection and flow over waves. PhD thesis, ETH Zurich, Switzerland, Diss. ETH 14359. Electronic version: http://e-collection.ethbib.ethz.ch/cgi.binshow.pl?type=diss&nr=14359

Günther, A. & Rudolf von Rohr, Ph. 2002 Structure of the temperature field for flow over heated waves. *Exps. Fluids* **33**, 920–930.

Henn, D. S. & Sykes, R. I. 1999 Large-eddy simulation of flow over wavy surfaces. *J. Fluid Mech.* **382**, 75–112.

Herzog, S. 1986 The large scale structure in the near-wall region of turbulent pipe flow. PhD thesis, Cornell University.

Hino, M. & Okumura, T. 1993 Coherent structure of turbulent flow over wavy walls. *Ninth Symp. on Turbulent Shear Flows, Kyoto*, pp. 14.3.1–14.3.4.

Hsu, S. T. & Kennedy, J. F. 1971 Turbulent flow in wavy pipes. *J. Fluid Mech.* **47**, 481–502.

Hudson, J. D. 1993 The effect of a wavy boundary on a turbulent flow. PhD thesis, University of Illinois, Urbana.

Hudson, J. D., Dykhno, L. & Hanratty, T. J. 1996 Turbulence production in flow over a wavy wall. *Exps. Fluids.* **20**, 257–265.

Kendall, J. M. 1970 The turbulent boundary layer over a wall with progressive surface waves. *J. Fluid Mech.* **41**, 259–281.

Krettenauer, K. & Schumann, U. 1992 Numerical simulation of turbulent convection over wavy terrain. *J. Fluid Mech.* **237**, 261–299.

Kuzan, J. D. 1986 Velocity measurements for turbulent separated and near separated flow over solid waves. PhD thesis, University of Illinois, Urbana.

Kuzan, J. D. & Hanratty, T. J. 1989 Turbulent flow with incipient separation over solid waves. *Exps. Fluids* **7**, 88–98.

Lees, L., Kubota, T. & Sigal, A. 1972 Stability theory for cross-hatching. Part II. An experiment on turbulent boundary layer over a wavy wall. *Tech. Rep.* SAMSO TR 72-34, vol. II, US Air Force.

Lin, J. C., Walsh, M. J., Watson, R. D. & Balasubramanian, R. 1983 Turbulent drag characteristic of small amplitude rigid surface waves. *AIAA Paper* 83-0228.

Liu, Z.-C., Adrian, R. J. & Hanratty, T. J. 2001 Large-scale modes of turbulent channel flow: Transport and structure. *J. Fluid Mech.* **448**, 53–80.

Lombardi, P., Angelis, V. D., Banerjee, S. 1996 Direct numerical simulation of near-interface turbulence in coupled gas-liquid flow. *Phys. Fluids* **8**, 1643.

Maass, C. & Schumann, U. 1996 Direct numerical simulation of separated turbulent flow over a wavy boundary. In *Flow Simulation with High Performance Computers* (ed. E. H. Hirschel). Notes on Numerical Fluid Mechanics, vol. 52, pp 227–241.

Markatos, N. C. G. 1978 Stochastic modeling of dynamic properties of non-linear water-waves. *Appl. Math. Modeling* **2**, 227–238.

Miles, J. W. 1957 On the generation of surface waves by shear flows *J. Fluid Mech.* **3**, 185–204.

Miller, C. A. 1995 Turbulent boundary layer above complex terrain PhD thesis, University of Western Ontario.

Motzfeld, H. 1937 Die turbulente Strömung an welligen Wänden. *Z. Angew. Math. Mech.* **47**, 193–212.

Nakagawa, S. & Hanratty, T. J. 2001 Particle image velocimetry measurements of flow over a wavy wall. *Phys. Fluids* **13**, 3504–3507.

Niederschulte, M. A. 1988 Turbulent flow through a rectangular channel. PhD thesis, University of Illinois.

Niederschulte, M. A., Adrian, R. J. & Hanratty, T. J. 1990 Measurements of turbulent flow in a channel at low Reynolds numbers. *Exps. Fluids* **8**, 222–231.

Patel, V. C., Chon, J. T. & Yoon, J. Y. 1991 Turbulent flow in a channel with a wavy wall. *Trans. ASME: J. Fluids Engng* **113**, 579–586.

Phillips, W. R. C. & Wu, Z. 1994 On the instability of wave-catalysed longitudinal vortices in strong shear. *J. Fluid Mech.* **272**, 235–254.

Phillips, W. R. C., Wu, Z. & Lumley, J. L. 1996 On the formation of longitudinal vorticies in a turbulent boundary layer over wavy terrain. *J. Fluid Mech.* **326**, 321–341.

Raupach, M. R., Antonia, R. A. & Rajagopalan, S. 1991 Rough-wall turbulent boundary layers. *Appl. Mech. Rev.* **44**, 1–25.

Robinson, S. K. 1991 Coherent motions in the turbulent boundary layer. *Annu. Rev. Fluid Mech.* **23**, 601–639.

Russ, G. & Beer, H. 1997 Heat transfer and flow field in a pipe with sinusoidal wavy surface-II. Experimental investigation. *Intl J. Heat Mass Transfer* **40**, 1071–1081.

Saric, W. S. 1994 Görtler vortices. *Annu. Rev. Fluid Mech.* **26**, 379–409.

Sigal, A. 1971 An experimantal investigation of the turbulent boundary layer over a wavy wall. PhD thesis, California Institute of Technology.

Sirovich, L. 1987 Coherent structures and chaos: a model problem. *Phys. Lett.* A **15**, 211–214.

Stanton, T., Marshall, D. & Houghton, R. 1932 The growth of waves on water due to the action of wind. *Proc. R. Soc. Lond.* A **137**, 283–293.

Stüer, H. 1999 Investigation of separation on a forward facing step. PhD thesis, Swiss Federal Institute of Technology (ETH), Diss. ETH No. 13132.

Thorsness, C. B. 1975 Transport phenomena associated with flow over a solid wavy surface. PhD thesis, University of Illinois, Urbana.

Weng, W., Chan, L., Taylor, P. A. & Xu, D. 1997 Modelling stably stratified boundary-layer flow over low hills. *Q. J. R. Met. Soc.* **123**, 1841–1866.

Westerweel, J. 1993 Digital particle image velocimetry. Theory and application. PhD thesis, Delft University of Technology.

Zagustin, K., Hsu, E. Y., Street, R. L. & Perry, B. 1966 Flow over a moving boundary in relation to wind-generated waves. *Tech. Rep.* 60, Contract NONR 225(71), Task NR 062-320, Stanford University.

Zilker, D. P. Jr 1976 Flow over wavy surfaces. PhD thesis, University of Illinois, Urbana.